

How To Find Charm in Nuclear Collisions at RHIC and LHC

S. Gavin,^{a,1} P. L. McGaughey,^b P. V. Ruuskanen,^c and R. Vogt^{d,e,2}

^aPhysics Department, Brookhaven National Laboratory, Upton, NY 11973

^bLos Alamos National Laboratory, Los Alamos, NM 87545

^cDepartment of Physics, University of Jyväskylä, Jyväskylä, Finland

^dNuclear Science Division, Lawrence Berkeley National Laboratory, Berkeley, CA 94720

^ePhysics Department, University of California at Davis, Davis, CA 95616

Abstract

Measurements of dilepton production from charm decay and Drell-Yan processes respectively probe the gluon and sea quark distributions in hadronic collisions. In nucleus-nucleus collisions, these hard scattering processes constitute a ‘background’ to thermal contributions from the hot matter produced by the collision. To determine the magnitude and behavior of this background, we calculate the hard scattering contribution to dilepton production in nuclear collisions at RHIC and LHC at next to leading order in perturbative QCD. Invariant mass, rapidity and transverse momentum distributions are presented. We compare these results to optimistic hydrodynamic estimates of the thermal dilepton production. We find that charm production from hard scattering is by far the dominant contribution. Experiments therefore can measure the gluon distribution in the nuclear target and projectile and, consequently, can provide new information on gluon shadowing. We then illustrate how experimental cuts on the rapidity gap between the leptons can aid in reducing the charm background, thereby enhancing thermal information.

PACS: 12.38.Mh, 25.75.+r

¹This manuscript has been authored under contract number DE-AC02-76CH00016 with the U. S. Department of Energy. Accordingly, the U.S. Government retains a non-exclusive, royalty-free license to publish or reproduce the published form of this contribution, or allow others to do so, for U.S. Government purposes.

²This work was supported in part by the Director, Office of Energy Research, Division of Nuclear Physics of the Office of High Energy and Nuclear Physics of the U. S. Department of Energy under Contract Number DE-AC03-76SF0098.

1 Introduction

Dilepton production provides an important tool for measuring the temperature of the high density matter produced in the early stages of a relativistic heavy-ion collision (see [1] and references therein). To make use of this tool at ion colliders such as RHIC and LHC, we must understand additional sources of dileptons from hard scattering and other non-equilibrium processes. In high energy pp interactions, the continuum in the dilepton mass range above $M \sim 2$ GeV is dominated by the Drell-Yan process and by semileptonic decays of D and other charm mesons. These leptons are produced by hard scatterings, at scales exceeding M and $2m_c \sim 3$ GeV respectively, so that their production can be addressed using perturbative QCD. In contrast, the lower mass region arises from soft processes, for which theory offers little guidance. We therefore hope to find a signal of thermal dilepton production at masses $M \sim 2 - 3$ GeV where *i*) the thermal contribution can still be sizable and *ii*) the background is calculable.

In this paper, we compare the predictions of dilepton production from a simple thermal model with the hard ‘background’ from heavy quark pair, $Q\bar{Q}$, decays and Drell-Yan production at RHIC and LHC nucleus-nucleus collision energies, $\sqrt{s} = 200$ GeV and 5.5 TeV in the nucleon-nucleon center of mass. Previously we compared the thermal dilepton and thermal charm rapidity distributions with Drell-Yan and initial charm production [1] calculated at leading order (LO). Our new next-to-leading order (NLO) results, shown to agree with pp and $p\bar{p}$ data in [2, 3], no longer depend on arbitrary phenomenological ‘K factors’ (often incorrectly taken to be ‘2’ in the literature). The remaining uncertainties in the NLO perturbative approach are well defined and likely rather small [2]. Also new to this paper are calculations of the invariant mass and transverse momentum distributions of the lepton pairs. We use these distributions to illustrate how thermal and hard dileptons can be distinguished in an experiment. In addition, we introduce the dilepton contribution from B meson decays, and discuss the effects of nuclear shadowing on the initial production.

Figure 1 shows the invariant mass distributions of the calculated contributions to the dilepton continuum in central nucleus-nucleus collisions at RHIC and LHC. We find that hard charm quark production and decay dominates the continuum below the Υ mass. In particular, the charm signal is more than an order of magnitude above the optimistic thermal dilepton and thermal charm rates for $M > 2$ GeV. This result implies that dilepton measurements can be used to extract the low x gluon density in the nucleus (see also [4]). On the other hand, the isolation of thermal signals will not be straightforward.

Additional complications can arise from the fact that the charm production cross section is large enough for multiple $D\bar{D}$ pairs to be produced in a single nucleus-nucleus collision. Uncorrelated pairs form when a lepton l^+ from one $D\bar{D}$ is randomly paired with a l^- from another $D\bar{D}$; the correlated signal in Fig. 1 includes only dileptons from $D\bar{D}$ pairs in which both quarks decay to leptons. In central Au+Au collisions at RHIC, up to 67 uncorrelated pairs may be produced while at the LHC, over 3000 uncorrelated pairs will contribute to the raw continuum from Pb+Pb collisions. Uncorrelated charm does not affect the measurement of parton densities, but it further complicates the task of extracting thermal information. Ideally the uncorrelated pairs can be removed by a

like-sign subtraction, leaving only the pairs shown in Fig. 1. Whether this subtraction can hold at the accuracy needed to extract thermal signals is another matter.

To enhance the thermal signal in an experiment, one can choose to count only those lepton pairs that have a small separation in rapidity. As observed by Fischer and Geist, dilepton pairs from charm decays typically occur with a large rapidity gap [5]. No such gap is present in Drell-Yan pairs or – importantly – in thermal pairs. Together with like sign subtraction, we expect that rapidity gap cuts can essentially remove the uncorrelated charm contamination and greatly suppress the correlated charm background. Indeed, the finite acceptance of a real detector can serve a similar purpose. We show that the acceptance window of PHENIX/RHIC and ALICE/LHC can enhance the signal from thermal charm decays to the point of measurability by rejecting pairs with large gaps.

This paper is organized as follows: In section 2, we discuss in detail Drell-Yan, $D\bar{D}$, and $B\bar{B}$ production in pp interactions and comment on how these results may be modified by nuclear shadowing. In section 3, we show the results for thermal dilepton and thermal $D\bar{D}$ pair production at RHIC and LHC, assuming the most optimistic scenario for the initial conditions to maximize the thermal rate. We compare the initial hard production of dileptons to the thermal model results in section 4. We discuss the effects of realistic detector geometries on the dilepton spectra at RHIC and LHC and draw our conclusions.

2 Dilepton Production from Initial Interactions

Perturbative QCD calculations of Drell-Yan and heavy quark production at leading order have long been available. The LO calculations differed from the experimental measurements by a K -factor ($K = \sigma^{\text{exp}}/\sigma^{\text{theory}}$) of 2-3 for charm production and 1.5-2 for Drell-Yan production. This difference suggested that higher order corrections to the production cross sections were important. Additionally, while multiplying the leading order cross section by a K factor describes the single-inclusive quark distributions as well as the mass and rapidity distributions of Drell-Yan and $Q\bar{Q}$ pairs, the pair p_T distributions for both processes are trivial at leading order since the pairs are produced back-to-back. Therefore next-to-leading order calculations are necessary to fully describe hard dilepton production.

In our previous work [1] we used the LO cross sections. Since then, an NLO treatment of $Q\bar{Q}$ production has been made available [6]. An NLO treatment of the Drell-Yan p_T distribution is also now available [2, 7]. With the NLO description of the perturbative cross sections, we also use NLO evaluations of the parton densities. Our results are obtained using the MRS D-’ [8] parton densities¹, compatible with the low x data from HERA [10]. The MRS D-’ sea quark and gluon distributions grow $\propto x^{-1/2}$ at the initial scale, $Q_0^2 = 5 \text{ GeV}^2$, when $x \rightarrow 0$. Using recent parton distribution functions that agree with the HERA data produces a substantial increase over our previous results [1], obtained with obsolete leading order parton distributions that become constant at Q_0^2 as $x \rightarrow 0$. Observe that older parton distributions such as [11] substantially underestimate the initial

¹All available parton distribution functions are contained in the package PDFLIB [9], available in the CERN library routines.

Drell-Yan and $Q\bar{Q}$ production at heavy-ion colliders.

We remark that updated versions of the MRS distributions are available, including MRS G [12] which has a slower low x growth than MRS D-'. While small, the changes from D-' to G affect our charm results most strongly. Compared to D-', we find that charm rates from G are 5% larger at RHIC and 20% smaller at LHC. No doubt, these numbers will continue to improve at that level as more data is analyzed, both from HERA and from Fermilab [13].

While the NLO evolution generally improves the agreement between the theory and the data, additional uncertainties are introduced, including dependence on scale and scheme. At fixed order in perturbation theory, the calculations depend on the renormalization scale and the factorization scale as well as the regularization scheme ($\overline{\text{MS}}$ or DIS). The hard scattering matrix elements and the definition of the parton densities for each process are specified by the regularization scheme. In this paper, we have used the $\overline{\text{MS}}$ scheme. The renormalization scale enters into the strong coupling constant, α_s , and the partonic cross sections while the parton distributions are evaluated at the factorization scale. The precise relationship between these scales and the momentum transfer, Q , is not uniquely defined. However, since the parton densities are analyzed assuming that they are equivalent, we also assume this. If the perturbative expansion converges, further higher-order corrections are small at large enough values of the scale μ . For such scales the physical cross section should become independent of the scale and scheme when calculated at higher and higher orders. If the μ dependence is strong, the perturbative calculation at that order is unreliable and further higher-order corrections are necessary [14]. The rates from the initial hard scatterings are rather sensitive to the scale and scheme in the moderate mass and p_T regime relevant to heavy-ion experiments.

Another uncertainty in our results involves the nuclear dependence of hard processes. When the charged parton distributions are probed in deep-inelastic scattering with a nuclear target and compared to a deuterium target, the ratio $R_{F_2} = F_2^A/F_2^D$ has a characteristic shape as a function of x . A depletion in the nucleus is observed at low x , the shadowing region, and intermediate x , the EMC region. Shadowing occurs in the region below $x \sim 0.1$ while the EMC region refers to $0.3 < x < 0.7$. Between the shadowing and EMC regions, $R_{F_2} > 1$, referred to as antishadowing. Although the origin of this behavior is not well understood, it is postulated to be either an interplay of coherent and incoherent multiple scatterings in the target or a modification of the parton densities in nuclear matter. In any case, the effect can be modeled phenomenologically by a parameterization to fit the nuclear deep-inelastic scattering data and implemented by a modification of the parton distributions in the nucleus. In the appendix, we choose two different parameterizations of the nuclear parton densities to illustrate the effect in AA collisions at RHIC and LHC. The first is a general fit to the most recent nuclear target data [15] that does not differentiate between quark, antiquark, and gluon modifications and does not include evolution in Q^2 . The second modifies the valence and sea quark and gluon distributions separately and includes Q^2 evolution [16] but is based on a fit to somewhat older data using obsolete parton densities. We find that at RHIC energies the charm and Drell-Yan yields may be reduced 40-50% while the bottom yield is changed by $\approx 10\%$. At the LHC, all the yields are reduced 50-60%. The results depend on the x

region probed and, in the case of the second parameterization, the scale Q^2 .

2.1 Drell-Yan Production

A detailed discussion of Drell-Yan production in high-energy NN collisions can be found in Ref. [2]. We repeat some of the pertinent points here. At leading order, Drell-Yan pairs are produced by $q\bar{q}$ annihilation into a virtual photon which decays to a lepton pair, $q\bar{q} \rightarrow \gamma^* \rightarrow l^+l^-$. The production cross section for lepton pairs with invariant mass, M , and rapidity y , summed over quark flavor f is

$$M^2 \frac{d\sigma_{\text{DY}}}{dydM^2} = \hat{\sigma}_0 \tau \sum_f e_f^2 [q_f(x_1, \mu) \bar{q}_f(x_2, \mu) + (1 \rightarrow 2)] , \quad (1)$$

where $\hat{\sigma}_0 = 4\pi\alpha^2/9M^2$ is the LO $q\bar{q}$ annihilation cross section, $\tau = M^2/s$, μ is the scale, and $x_{1,2} = \sqrt{\tau}e^{\pm y}$ are the projectile and target momentum fractions at which the parton densities are evaluated. For $y > 0$, x_1 increases with rapidity while x_2 decreases. At NLO, the Compton and annihilation processes $qg \rightarrow q\gamma^*$ and $q\bar{q} \rightarrow g\gamma^*$ contribute in addition to vertex corrections to the LO cross section so that eq. (1) is replaced with

$$\begin{aligned} M^2 \frac{d\sigma}{dydM^2} &= \hat{\sigma}_0 \tau \int_0^1 dx_1 dx_2 dz \delta(x_1 x_2 z - \tau) \delta\left(y - \frac{1}{2} \ln\left(\frac{x_1}{x_2}\right)\right) \\ &\times \left\{ \left[\sum_f e_f^2 [q_f(x_1, \mu) \bar{q}_f(x_2, \mu) + (1 \rightarrow 2)] \right] \left[\delta(1-z) + \frac{\alpha_s(\mu)}{2\pi} f_q(z) \right] \right. \\ &\left. + \left[\sum_f e_f^2 [g(x_1, \mu)(q_f(x_2, \mu) + \bar{q}_f(x_2, \mu)) + (1 \rightarrow 2)] \right] \left[\frac{\alpha_s(\mu)}{2\pi} f_g(z) \right] \right\} . \end{aligned} \quad (2)$$

Note that going to NLO requires a redefinition of x_1 and x_2 since the unobserved parton contributes to the total momentum in the final state. The correction terms f_q and f_g are regularization scheme dependent. The scale and scheme dependences are not large for $M > 4$ GeV. We will only consider Drell-Yan production for $M \geq 2$ GeV since below this value the perturbative calculation becomes unreliable. The mass and rapidity distributions were calculated using a program provided by Rijken and van Neerven [17].

The p_T dependence is trivial at LO — the lepton pair has $p_T = 0$ if no intrinsic parton p_T is included. Some of the Drell-Yan pair transverse momentum can be accounted for by introducing a soft intrinsic p_T distribution with $\langle p_T \rangle \sim 0.3$ GeV. However, this is too small to account for the measured p_T distributions with $\langle p_T \rangle \sim 1$ GeV at $M = 10$ GeV. At NLO, the pair acquires transverse momentum through recoil of the virtual photon with the final-state parton. Here the p_T dependence can be calculated perturbatively and is well behaved for $p_T \sim M$. However, at low p_T , the perturbative expansion parameter, $\alpha_s \ln^2(M^2/p_T^2)$, becomes large and the expansion breaks down, making it necessary to resum the perturbation series. The resulting cross section is

$$M^2 \frac{d\sigma_{\text{resum}}}{dp_T^2 dy dM^2} = \pi \hat{\sigma}_0 \tau e_q^2 \int \frac{d^2b}{(2\pi)^2} e^{i\mathbf{b} \cdot \mathbf{p}_T} W(b) , \quad (3)$$

where a Fourier transformation is made to impact parameter space and the form factor, $W(b)$, effectively sums the leading and sub-leading logarithms. The p_T distributions have been calculated using a code developed by Arnold and Kauffman for $p\bar{p} \rightarrow W, Z$ [7] and extended to Drell Yan in pp collisions in [2]. This code includes a method of interpolating between the low and high p_T behavior.

The number of Drell-Yan pairs of mass M produced in central nucleus-nucleus collisions,

$$\frac{dN_{\text{DY}}}{dM} = T_{AB}(0) \frac{d\sigma_{\text{DY}}}{dM}, \quad (4)$$

is always small in the range where the perturbative calculation is expected to be applicable, *i.e.* $M > 2$ GeV. However, only a calculation of the mass-integrated cross section can reveal whether or not the AB rate is large enough for false Drell-Yan pair production to be a problem. Since such a calculation is not possible over all masses, experimental techniques must be used to insure that these uncorrelated Drell-Yan pairs do not contaminate the spectrum. For example, a p_T cutoff should reduce the probability of false high mass Drell-Yan pairs arising from low mass pairs with large rapidity separation. Additionally, a study of the angular distribution would also reduce any uncorrelated Drell-Yan pairs. The number of lepton pairs in central Au+Au collisions at $M = 2, 4,$ and 6 GeV are given in Table 1 for RHIC and in Table 2 for central Pb+Pb collisions at the LHC. They are significantly larger than in our previous work [1] due to the different small x behavior of the parton densities. The average mass and p_T of the Drell-Yan pairs (with $M > 2$ GeV) produced at RHIC and LHC energies are shown in Table 3.

Figures 2 and 3 show the NLO rates for Au+Au collisions at RHIC and Pb+Pb collisions at the LHC. The calculated p_T distributions for $M = 4$ and 6 GeV at $y = 0$ and 2 are shown in Figs. 2(a) and 3(a). The distributions at higher rapidity are nearly parallel until the kinematic limit is approached. Given this, we have assumed that the p_T distribution has the same shape for $M = 2$ GeV and scaled the 4 GeV results to obtain the p_T distribution at $M = 2$ GeV. The rapidity distributions are shown in Fig. 2(c) for RHIC energies and 3(c) for the LHC. The cross section grows with rapidity until the kinematic limit is approached because $x_2\bar{q}(x_2, \mu)$ increases and $x_1q(x_1, \mu)$ decreases with increasing y . As previously discussed, the parton density dependence is enhanced for low masses and high rapidities at $\sqrt{s} = 5.5$ TeV even though the rapidity-integrated results do not depend strongly on the parton densities. Note that the strongest dependence on the parton densities occurs outside the range of current measurements. In our previous work, the variation with rapidity was weaker because we used obsolete parton distributions where $x\bar{q}(x \rightarrow 0, Q_0^2) \rightarrow \text{constant}$.

2.2 Heavy Quark Production and Decay

At RHIC and LHC energies, heavy quark production will be substantial. We consider both charm and bottom production and fragmentation into heavy mesons which subsequently decay to lepton pairs. The double differential heavy meson pair production cross section

at LO is [18, 19]

$$E_H E_{\overline{H}} \frac{d\sigma_{H\overline{H}}}{d^3p_H d^3p_{\overline{H}}} = \int \frac{\hat{s}}{2\pi} \frac{dx_1}{x_1} \frac{dx_2}{x_2} dz_H dz_{\overline{H}} C(x_1, x_2) \frac{E_H E_{\overline{H}}}{E_Q E_{\overline{Q}}} \quad (5)$$

$$\frac{D_{Q/H}(z_H) D_{\overline{Q}/\overline{H}}(z_{\overline{H}})}{z_H^3 z_{\overline{H}}^3} \delta^4(p_1 + p_2 - p_Q - p_{\overline{Q}}) ,$$

where $H(Q\overline{q})\overline{H}(\overline{Q}q)$ is the heavy meson pair, $D\overline{D}$ for $Q = c$ and $B\overline{B}$ for $Q = b$. The fragmentation function, $D_{Q/H}(z)$, describes the hadronization of the heavy quarks where $z = p_H/p_Q$ is the fractional momentum of the heavy quark carried by the hadron. Charm hadroproduction at low p_T is best described by the assumption that the charmed quark experiences no momentum loss during hadronization, *i.e.* $D_{Q/H}(z) = \delta(1 - z)$ [18], resulting in a shift between y_Q and y_H due to the quark and meson mass difference. At LO heavy quarks are produced by gluon fusion, $gg \rightarrow Q\overline{Q}$, and quark-antiquark annihilation, $q\overline{q} \rightarrow Q\overline{Q}$. To LO, the convolution function $C(x_1, x_2)$ is

$$C(x_1, x_2) = \sum_f [x_1 q_f(x_1, \mu) x_2 \overline{q}_f(x_2, \mu) + x_1 \overline{q}_f(x_1, \mu) x_2 q_f(x_2, \mu)] \frac{d\hat{\sigma}(x_1, x_2, \mu)}{d\hat{t}} \Big|_{q\overline{q}} \quad (6)$$

$$+ x_1 g(x_1, \mu) x_2 g(x_2, \mu) \frac{d\hat{\sigma}(x_1, x_2, \mu)}{d\hat{t}} \Big|_{gg} ,$$

where $d\hat{\sigma}/d\hat{t}$ can be found in *e.g.* [3, 14].

The NLO, order α_s^3 , corrections to $Q\overline{Q}$ production have been calculated for the total cross section [20], single-inclusive quark distributions [21, 22], and exclusive $Q\overline{Q}$ pair distributions [6]. In addition to real and virtual corrections to the LO processes, quark-gluon scattering, $q(\overline{q})g \rightarrow Q\overline{Q}q(\overline{q})$ is also included². The total partonic cross section, $\hat{\sigma}_{ij}$, can be expressed as

$$\hat{\sigma}_{ij}(x_1 x_2 s, m_Q, \mu) = \frac{\alpha_s^2(\mu)}{m_Q^2} \left\{ f_{ij}^0(\rho) + \frac{\alpha_s(\mu)}{4\pi} [f_{ij}^1(\rho) + \overline{f}_{ij}^1(\rho) \ln(\mu^2/m_Q^2)] + \mathcal{O}(\alpha_s^2) \right\} , \quad (7)$$

where $\rho = 4m_Q^2/x_1 x_2 s$ and $f_{qg}^0 = 0$. The double differential meson pair production cross section to NLO is then

$$E_H E_{\overline{H}} \frac{d\sigma_{H\overline{H}}}{d^3p_H d^3p_{\overline{H}}} = \sum_{i,j} \int dx_1 dx_2 dz_H dz_{\overline{H}} \frac{E_H E_{\overline{H}}}{E_Q E_{\overline{Q}}} \frac{D_{Q/H}(z_H) D_{\overline{Q}/\overline{H}}(z_{\overline{H}})}{z_H^3 z_{\overline{H}}^3} \quad (8)$$

$$\left[\frac{E_Q E_{\overline{Q}}}{d^3p_H d^3p_{\overline{H}}} \frac{d\hat{\sigma}_{ij}(x_1 x_2 s, m_Q, \mu)}{d^3p_H d^3p_{\overline{H}}} \right] q_i(x_1, \mu) q_j(x_2, \mu) ,$$

where q_i and q_j are the quark, antiquark and gluon densities, appropriately defined in the particular scheme. The sum runs over gg fusion, $q\overline{q}$ annihilation and $q(\overline{q})g$ scattering. The NLO corrections become large when $m_Q/\sqrt{s} \ll 1$ since gluon exchange dominates

²This process has been interpreted at LO as the scattering of a heavy quark excited from the nucleon sea with a light quark or gluon, *e.g.* $gQ \rightarrow gQ$, and is referred to as flavor excitation [14, 20]. However, for moderate p_T , flavor excitation is suppressed at LO due to the small heavy quark parton density near threshold.

the asymptotic behavior. However, the perturbative expansion may still be valid if further higher-order corrections are small.

The $c\bar{c}$ total cross section at NLO, $\sigma_{c\bar{c}}^{\text{tot}}$, has been compared with pp and pA data at $\sqrt{s} \leq 63$ GeV [23, 24], assuming a linear nuclear dependence [25, 26, 27], to fix m_c and μ and provide an extrapolation to collider energies [3]. Reasonable agreement with the data was found for $m_c = 1.2$ GeV and $\mu = 2m_c$ for MRS D- $'$, leading to $\sigma_{c\bar{c}}^{\text{tot}} = 344 \mu\text{b}$ at RHIC and 17.7 mb at the LHC. We use $m_b = \mu = 4.75$ GeV to calculate $b\bar{b}$ production, finding $\sigma_{b\bar{b}}^{\text{tot}} = 1.5 \mu\text{b}$ at RHIC and 224 μb at the LHC. The $c\bar{c}$ cross sections are larger than earlier estimates [1] because of the low x behavior of the gluon distributions³. However, the theoretical K factor, $\sigma_{Q\bar{Q}}^{\text{NLO}}/\sigma_{Q\bar{Q}}^{\text{LO}} \sim 2-3$, is rather large, particularly for $c\bar{c}$, suggesting that the perturbative expansion is unreliable for $m_Q/\sqrt{s} \ll 1$. For details of the calculation and the theoretical uncertainties, see [3, 29].

It was recently shown that when $\mu \propto m_T$, the theoretical K factor is nearly constant for distributions that are nontrivial at LO [29]⁴. Therefore, the NLO calculation is essential only for the pair p_T and azimuthal distributions. We calculate the meson pair invariant mass distributions and the double differential rapidity and rapidity gap, $y_g = y_H - y_{\bar{H}}$, distributions $d\sigma_{H\bar{H}}/dydM$ and $d\sigma_{H\bar{H}}/dy_gdM$ at LO assuming $D_{Q/H}(z) = \delta(1-z)$ and checked that our results agreed with the LO results from the program of Nason and collaborators [6]. The rapidity gap is needed for acceptance studies since the mesons decay independently. The total cross section and $Q\bar{Q}$ pair p_T distributions are calculated at NLO using the same program [6]. We note that, so far, no resummation of the $Q\bar{Q}$ p_T distribution has been performed for low p_T , analogous to Drell-Yan production (see eq. (3) and [2, 7]). Therefore, we have only shown the $Q\bar{Q}$ p_T distribution where the calculation may be considered to be reliable. The $Q\bar{Q}$ and $H\bar{H}$ p_T distributions are assumed to be equal, in keeping with the trivial fragmentation function used for the longitudinal momentum distribution [18]. At large p_T , this is no longer a good approximation. However, in the low p_T region, of interest in heavy-ion collisions, this assumption should be reasonable. We assume no intrinsic light parton p_T in the parton densities and integrate over x_1 and x_2 using four-momentum conservation. The triple differential cross section, eq. (5) is then

$$\frac{d\sigma_{H\bar{H}}}{dydy_gdM^2} = \frac{\sigma_{\text{NLO}}}{\sigma_{\text{LO}}} \int dp_{T,Q}^2 dz_H dz_{\bar{H}} dy_H dy_{\bar{H}} C(x_1, x_2) \frac{E_H E_{\bar{H}}}{E_Q E_{\bar{Q}}} \frac{D_{Q/H}(z_H) D_{\bar{Q}/\bar{H}}(z_{\bar{H}})}{z_H z_{\bar{H}}} \delta(y - (y_H + y_{\bar{H}})/2) \delta(M^2 - (p_H + p_{\bar{H}})^2) \delta(y_g - y_H + y_{\bar{H}}), \quad (9)$$

where $\sigma_{\text{NLO}}/\sigma_{\text{LO}}$ is the theoretical K factor. The definition of the pair rapidity, $y = (y_H + y_{\bar{H}})/2$, holds when $p_{T,Q} = p_{T,\bar{Q}}$ which is true when the initial parton p_T is neglected.

If the average number of $H\bar{H}$ pairs,

$$N_{H\bar{H}} = T_{AB}(0) \sigma_{H\bar{H}}, \quad (10)$$

³Choosing another parton density with a lower initial scale but similar small x behavior [28] leads to a somewhat smaller charm cross section at LHC, $\sigma_{c\bar{c}}^{\text{tot}} = 6.7$ mb while the $c\bar{c}$ cross section at RHIC is 351 μb , nearly independent of the choice of parton densities [3].

⁴Ref. [30] reaches a different conclusion with $\mu \propto m_Q$. However, this choice introduces large logarithms for $p_T \geq m_Q$, making the calculation unstable.

produced in central collisions is small, $N_{H\bar{H}} \ll 1$, the lepton pairs will be correlated with $N_l^{\text{corr}} = N_{H\bar{H}} B_R^2(H/\bar{H} \rightarrow l^\pm X)$. However, if $N_{H\bar{H}} > 1$, opposite sign lepton pairs from uncorrelated $H\bar{H}$ pair decays need to be taken into account. When $N_{H\bar{H}} \gg 1$, the average number of uncorrelated lepton pairs is $N_l^{\text{uncorr}} = N_{H\bar{H}}(N_{H\bar{H}} - 1) B_R^2(H\bar{H} \rightarrow l^\pm X)$. If $N_{H\bar{H}} \approx 1$, a distribution in $N_{H\bar{H}}$ must be considered to calculate the uncorrelated pairs.

The $c\bar{c}$ production cross sections are large enough for lepton pair production from uncorrelated $D\bar{D}$ decays to be substantial in nuclear collisions, particularly at the LHC. Given our values of $\sigma_{c\bar{c}}^{\text{tot}}$ and assuming that all $c\bar{c}$ pairs produce final-state $D\bar{D}$ pairs, we find $N_{D\bar{D}} \sim 8.7$ at RHIC and $N_{D\bar{D}} \sim 450$ at the LHC⁵. Up to 3100 uncorrelated pairs can be formed among the $B_R(D \rightarrow l^+ X) N_{D\bar{D}} \sim 55$ l^+ and l^- leptons from the charm decays in central Pb+Pb collisions at the LHC.

In Figs. 4 and 5 we show the rates of $c\bar{c}$ and $D\bar{D}$ production at RHIC and LHC as a function of p_T , M , y_g , and y . The $b\bar{b}$ and $B\bar{B}$ rates are given in Figs. 6 and 7. The meson pair rapidity distributions are somewhat narrower than the corresponding quark pair distributions due to the quark and meson mass differences. The rapidity gap increases with M and $dN/dy_g dM$ has a minimum at $y_g = 0$ since for fixed mass, $M^2 = 2m_T^2(1 + \cosh y_g)$, small y_g corresponds to large p_T . However, the mass integrated rapidity gap distribution, dN/dy_g , does not have a minimum at $y_g = 0$.

Lepton pairs from $D\bar{D}$ and $B\bar{B}$ decays have been obtained using a Monte Carlo code based on D decays measured by Mark-III [32] and B decays observed with CLEO [33]. Opposite sign lepton pairs can be produced from a single B decay by the chain $B \rightarrow \bar{D}l^+ X$, $\bar{D} \rightarrow l^- X$. Our calculation assumes that the lepton pairs result from the decay of the initial B and \bar{B} . Note that the CLEO analysis [33] assumes that the measured leptons are from the decays of the initial B 's rather than from secondary decays. However, if $B\bar{B}$ production is significant, the secondary decays in the chain could add a component to the low mass background. The inclusive branching ratio for D meson decay to leptons, averaged over charged and neutral D 's, is $B_R(D^0/D^+ \rightarrow l^+ X) \sim 12\%$ [34]. The corresponding branching ratio for B mesons of unspecified charge is $B_R(B \rightarrow l^+ X) \sim 12\%$ [34]. The momentum vectors of each meson are computed in the $H\bar{H}$ pair rest frame using the rapidity gap distribution, $dN/dy_g dM$, to separate the mesons. The decays are calculated in the meson rest frame according to the measured lepton momentum distributions [32, 33] and boosted back to the nucleon-nucleon center of mass frame where the lepton pair quantities are computed. To account for uncorrelated lepton pair production in the Monte Carlo code, two $H\bar{H}$ pairs are generated and the H from the first pair is decayed with the \bar{H} from the second.

The lepton pairs from correlated and uncorrelated $D\bar{D}$ decays are shown for central Au+Au collisions at RHIC and Pb+Pb collisions at LHC in Figs. 4 and 5. The number of lepton pairs from heavy quark decays at $M = 2, 4$, and 6 GeV are given in Table 1

⁵The $c\bar{c}$ production rate at LHC is compatible with an earlier estimate using the parton cascade model [31] where ~ 400 $c\bar{c}$ pairs are produced at $\sqrt{s} = 6.3$ TeV. However, our RHIC rate is considerably smaller than the 60 $c\bar{c}$ pairs predicted by the parton cascade. The discrepancy cannot be fully accounted for within the theoretical uncertainties. In fact, if we use the same parton densities as in the parton cascade model with the same charmed quark mass and scale, our production rate drops by a factor of two at the LHC but is unchanged at RHIC energies [3]. Therefore, initial $c\bar{c}$ production cannot be the only important source of charm in the parton cascade model.

for central Au+Au collisions at RHIC and in Table 2 for central Pb+Pb collisions at the LHC. Note that in obtaining the number of pairs from our Monte Carlo simulation, we average over mass bins of width 400 MeV. The average mass and p_T of the decay pairs produced at RHIC and LHC energies are shown in Table 3. The dileptons resulting from uncorrelated $D\bar{D}$ pairs have larger masses since the rapidity gap between the uncorrelated mesons is larger on average than between the correlated pairs. In fact the average mass of lepton pairs from uncorrelated $D\bar{D}$ decays is 30% larger than that of the correlated pairs at LHC. The average rapidity of the lepton pairs from uncorrelated $D\bar{D}$ decays is smaller than from correlated decays at the LHC whereas the average p_T is somewhat larger for the uncorrelated pairs. Uncorrelated $B\bar{B}$ decays have not been considered here but should produce only a relatively small enhancement at LHC for $M < 10$ GeV. We show the lepton pairs from correlated $B\bar{B}$ decays in Figs. 6 and 7. Note that, in general, the average lepton pair p_T increases with dilepton mass while the average lepton pair rapidity decreases with mass.

3 Dilepton Production by Thermal Processes

We now calculate the rates of thermal lepton pair production, both directly from thermal $q\bar{q}$ annihilation and from the decays of $D\bar{D}$ pairs produced thermally. We expect that the longitudinal expansion approximately follows the scaling law, $v_z = z/t$, at RHIC and LHC until large rapidities where particle densities become small and pressure gradients cause scaling violations. Numerical calculations [35, 36] give support for a picture where these deviations are small up to the fragmentation regions, therefore we neglect them here.

With the scaling ansatz for the longitudinal velocity we can relate the initial density and initial time to the final multiplicity distribution of hadrons by $n_i\tau_i = (dN/d\eta)/(\pi R_A^2)$. The temperature is therefore a function of η , $T_i \equiv T_i(\eta)$, where we can identify the fluid and particle rapidities since the overall rapidity distribution is much broader than the thermal distribution at freeze-out. We parametrize the multiplicity distribution in the form

$$\frac{dN}{d\eta} = \left(\frac{dN}{d\eta}\right)_0 \exp(-\eta^2/2\sigma^2), \quad (11)$$

where $(dN/d\eta)_0$ is the total multiplicity at $\eta = 0$ and σ measures the width of the hadron rapidity distribution. As before, [1] we assume the following initial conditions: at RHIC energies, $|\eta| \leq 6$ and we choose $(dN/d\eta)_0 = 2000$ while for the LHC $|\eta| \leq 8$ and we take $(dN/d\eta)_0 = 5000$. The width is estimated from the total energy of the final particles. We find $\sigma \sim 3$ at RHIC and at LHC, $\sigma \sim 5$. These rapidity densities, while somewhat high, are consistent with the (optimistic) high initial temperatures taken here, as well as with Parton Cascade Model calculations [31]. Like the scaling properties of the longitudinal velocity, the Gaussian form of the multiplicity distribution must break down at rapidities close to the phase space limit. There, however, the densities become too small for thermal production to be important.

3.1 Thermal Dileptons

In the quark-gluon plasma, lepton pairs are expected to be produced by the annihilation process $q\bar{q} \rightarrow \gamma^* \rightarrow l^+l^-$, similar to Drell-Yan production in the initial nucleon-nucleon interactions. However, in the plasma, the nuclear quark distributions are replaced by thermal distributions. Neglecting the transverse flow the dilepton emission rate is then [37, 38]

$$\frac{dN}{d^4x d^2p_T dy dM^2} = \frac{\alpha^2}{8\pi^4} F \exp[-(m_T \cosh(y - \eta)/T)] , \quad (12)$$

where T is the temperature and η is the rapidity of the medium. In a plasma, $F_Q = \sum e_q^2$, while in an equilibrium hadron gas, assuming $\pi\pi \rightarrow \rho \rightarrow l^+l^-$ is the dominant channel, $F_H = \frac{1}{12} m_\rho^4 / ((m_\rho^2 - M^2)^2 + m_\rho^2 \Gamma_\rho^2)$. The mixed phase has a fractional contribution from each with $F_M = f_0(r - 1) [f_0 F_Q + ((r - 2)f_0 + 2)F_H]$.

In addition to $\pi\pi \rightarrow \rho \rightarrow l^+l^-$ other hadronic processes contribute to the dilepton rate. In the region above the ρ mass they dominate [39] over the ρ contribution which is cut off by the form factor. The assumption that vector mesons saturate the $e^+e^- \rightarrow$ hadrons cross section indicates that at the phase transition temperature the dilepton rate in the hadron gas could be very similar to that from the quark-gluon plasma [40]. Neglecting these contributions underestimates the hadronic emission in the mass range between the ρ and J/ψ mesons.

The rapidity distribution for a given dilepton mass is

$$\begin{aligned} \frac{dN}{dM dy} = & \frac{\alpha^2}{2\pi^3} \pi R_A^2 \left\{ \theta(s_i - s_Q) \frac{3F_Q}{M^3} \int_{-Y}^Y \frac{d\eta (\tau_i T_i^3)^2}{\cosh^6(\eta - y)} P_1(x) e^{-x|_{x_c}} \right. \\ & + \theta(s_i - s_H) M^3 \frac{\tau_m^2}{2} F_M \int_{-Y}^Y d\eta \left(\frac{1}{x_c} + \frac{1}{x_c^2} \right) e^{-x_c} \\ & \left. + \theta(s_i - s_{\text{dec}}) \frac{3F_H}{M^3} \int_{-Y}^Y \frac{d\eta (\tau_H T_H^3)^2}{\cosh^6(\eta - y)} P_1(x) e^{-x|_{x_{\text{dec}}}} \right\} , \quad (13) \end{aligned}$$

where $P_1(x) = x^4 + 5x^3 + 15x^2 + 30x + 30$, $x = M \cosh(\eta - y)/T$, s_i is the initial entropy density and s_Q and s_H are the entropy densities of the plasma and the hadron gas at the transition temperature T_c . The invariant mass distribution is obtained by integrating eq. (13) over the rapidity interval $-Y \leq y \leq Y$. Likewise the transverse momentum distribution for mass M is

$$\begin{aligned} \frac{dN}{dM dp_T} = & \frac{\alpha^2}{2\pi^3} \pi R_A^2 M p_T \left\{ \theta(s_i - s_Q) 3F_Q \int_{-Y}^Y \frac{d\eta dy (\tau_i T_i^3)^2}{m_T^6 \cosh^6(\eta - y)} P_2(z) e^{-z|_{z_c}} \right. \\ & + \theta(s_i - s_H) \frac{\tau_m^2}{2} F_M \int_{-Y}^Y d\eta dy e^{-m_T \cosh(\eta - y)/T} \\ & \left. + \theta(s_i - s_{\text{dec}}) 3F_H \int_{-Y}^Y \frac{d\eta dy (\tau_H T_H^3)^2}{m_T^6 \cosh^6(\eta - y)} P_2(z) e^{-z|_{z_{\text{dec}}}} \right\} , \quad (14) \end{aligned}$$

where $P_2(z) = z^5 + 5z^4 + 20z^3 + 60z^2 + 120z + 120$ and $z = m_T \cosh(\eta - y)/T$.

As defaults, we assume a three-flavor plasma and a hadron gas of massless pions with $T_c = 200$ MeV and $T_{\text{dec}} = 140$ MeV. Then

$$s_i = \begin{cases} 4\gamma_k \frac{\pi^2}{90} T_i^3 & s_i > s_Q \text{ OR } s_i < s_H \\ f_0 s_Q + (1 - f_0) s_H & s_H < s_i < s_Q \end{cases}$$

where γ_k is the number of degrees of freedom with $\gamma_H = 3$ and $\gamma_Q = 16 + 21n_f/2$ and $n_i = s_i/3.6$. The beginning of the mixed phase occurs at

$$\tau_m = \begin{cases} \tau_i (T_i/T_c)^3 & T_i > T_c \\ 1 \text{ fm} & T_i = T_c \end{cases}.$$

The initial plasma content of the mixed phase is

$$f_0 = \begin{cases} 1 & T_i > T_c \\ (s_i - s_H)/(s_Q - s_H) & T_i = T_c \\ 0 & T_i < T_c \end{cases}.$$

The beginning of the hadron phase is then

$$\tau_H = \begin{cases} \tau_m r & T_i \geq T_c \\ 1 \text{ fm} & T_i < T_c \end{cases},$$

where $r = s_Q/s_H = \gamma_Q/\gamma_H$. There is no thermal contribution if $T_i < T_{\text{dec}}$.

In our previous work, we used three different hypotheses to fix T_i and τ_i [1]. Since here we wish to determine if any plasma contribution is observable at all, we focus on the highest temperature scenario, $\tau_i(3T_i) \simeq \hbar c$, yielding $T_{i,\text{max}} \sim 515$ at RHIC and 810 MeV at the LHC, similar to the results of Ref. [41]. The corresponding initial times are $\tau_i \sim 0.2$ fm and 0.08 fm respectively. Thermalization at such early times is a bold assumption, if taken literally. Following McLerran, Kapusta and Srivastava [41], we employ it to schematically characterize pre-equilibrium pair production [42, 43]. For our choice of initial conditions, plasma production dominates the thermal distributions over all observable phase space. However, other initial conditions with lower initial temperatures result in a much smaller thermal yield for $M \geq 2$ GeV. For example, if we choose instead $T_c = 150$ MeV and $T_{\text{dec}} = 100$ MeV, as recent lattice calculations with quarks indicate [44], then the hadron gas contribution is considerably reduced. Since we have assumed a high initial temperature and study pairs with $M \geq 2$ GeV only, the hadron contribution is a small fraction of the yield. At $M = 2$ GeV, the yield is reduced by $\sim 30\%$ with $T_c = 150$ MeV while higher masses are virtually unaffected. Reducing $(dN/d\eta)_0$ would reduce T_i , increasing the relative importance of the hadronic contribution and decreasing the plasma yield. Additionally, recent analyses of the initial conditions [45, 46] suggest that the quark density is too low for the quarks to be in chemical equilibrium. Therefore, even if the initial temperature is high, the dilepton yield would be significantly reduced because of the low quark density.

We neglect the transverse expansion and describe the matter in the longitudinal direction only. Transverse expansion mainly affects the later part of the mixed phase and the

hadron gas phase [47, 48]. If it is included, the contribution from the hadron gas phase is negligible for $M \geq 2$ GeV except at large rapidities where the initial density is too low to produce a plasma. Therefore a full three-dimensional hydrodynamic calculation would give a narrower thermal pair rapidity distribution than our longitudinal scaling approximation.

We have so far discussed the properties of the lepton pairs. However, once acceptance questions are addressed, it is necessary to track each lepton separately. The space-time integration remains the same, but now we write more generally

$$E \frac{dN}{d^4x d^3p dy_g dM^2} = \int \frac{d^3k_1}{E_{k_1}} \frac{d^3k_2}{E_{k_2}} \frac{d^3p_1}{E_{p_1}} \frac{d^3p_2}{E_{p_2}} f(k_1) f(k_2) \frac{36|\mathcal{M}|^2}{16(2\pi)^8} \delta^4(k_1 + k_2 - p_1 - p_2) \delta(M^2 - (p_1 + p_2)^2) \delta(y_g - y_{p_1} + y_{p_2}) \delta(\vec{p} - \vec{p}_1 - \vec{p}_2), \quad (15)$$

where k_1 and k_2 are the incoming quark and antiquark, p_1 and p_2 are the outgoing leptons, and $f(k)$ is the thermal (Boltzmann) distribution of the initial partons. Note that if the rapidity gap is integrated over, eq. (15) reduces to eq. (12). The p_T , mass, rapidity gap, and pair rapidity distributions for $M \geq 2$ GeV are shown in Figs. 8 and 9 for RHIC and LHC respectively. The number of thermal lepton pairs with $M = 2, 4,$ and 6 GeV are given in Tables 1 and 2 for central collisions at RHIC and LHC. The rapidity gap distribution, $dN/dy_g dM$ does not increase with y_g at fixed M as it does for the initial $Q\bar{Q}$ production because the thermal partons are not aligned along a particular direction. However, the average p_T and rapidity of the thermal distributions follows the trend of the heavy quark decays: $\langle p_T \rangle$ increases with mass while $\langle y \rangle$ decreases. The average thermal pair mass and p_T are shown in Table 3 for $M > 2$ GeV at RHIC and LHC.

3.2 Thermal Charm

With a large initial temperature in the most optimistic scenario, $T_{i,\max} \sim (1/3 - 1/2)m_c$, significant thermal charm production may be expected, as previously suggested [49, 50]. The thermal $c\bar{c}$ production rate can be found by making the replacement

$$36|\mathcal{M}_{q\bar{q} \rightarrow ll}|^2 \rightarrow \gamma_q |\mathcal{M}_{q\bar{q} \rightarrow c\bar{c}}|^2 + \gamma_g |\mathcal{M}_{gg \rightarrow c\bar{c}}|^2, \quad (16)$$

in eq. (15) where now p_1 and p_2 are the four-momenta of the charm quarks and the quark and gluon degeneracy factors are $\gamma_q = 3 \times (2 \times 3)^2$ for three quark flavors and $\gamma_g = (2 \times 8)^2/2$ (the factor of 1/2 is needed to prevent double counting) [50]. The matrix elements are given in [51]. We use $m_c = 1.2$ GeV to be consistent with the initial $c\bar{c}$ production calculations and include only plasma production⁶. The fragmentation of the charmed quarks into $D\bar{D}$ pairs has also been incorporated, as in eq. (5). We find approximately one thermal $D\bar{D}$ pair at RHIC and 23 pairs in Pb+Pb collisions at LHC. These results are essentially in agreement with those of the ideal thermal case discussed in [52] and [53]. The rate is high enough at the LHC for ≈ 500 lepton pairs to be produced

⁶In our previous paper [1], a normalization constant was left out of the calculation. The correction has the effect of reducing the thermal charm yield. Note also that a typographical factor of two is also missing from eq. (13) of that paper.

from uncorrelated decays. Again, an ideal background subtraction should remove the uncorrelated pairs.

The thermal charm and resulting $D\bar{D}$ distributions are shown in Figs. 10 and 11 along with the dilepton yields. The number of thermal lepton pairs with $M = 2, 4,$ and 6 GeV are given in Tables 1 and 2 for central collisions at RHIC and LHC. As before, the number of pairs at each mass is averaged over mass bins of width 400 MeV. The average $D\bar{D}$ pair mass and p_T are somewhat larger than the corresponding $c\bar{c}$ averages. The $D\bar{D}$ pair mass is 1.5 GeV larger while $\langle p_T \rangle$ is 400 MeV larger at RHIC and 600 MeV larger at LHC. These increases deplete high rapidity $D\bar{D}$ pairs with respect to $c\bar{c}$ production. The rapidity gap is also decreased, although not significantly. The average thermal pair mass and p_T are given in Table 3 for both RHIC and LHC. The mass and p_T distributions of lepton pairs resulting from correlated $D\bar{D}$ decays are similar in shape to the thermal dileptons and with a similar yield at the same lepton pair mass. However, the lepton pair rapidity distributions from $D\bar{D}$ decays are narrower. As in the case of initial $c\bar{c}$ production, the uncorrelated lepton pairs have a much broader mass distribution than the correlated pairs.

4 Results and Conclusions

4.1 Results

We now compare the perturbative lepton pair production with thermal production. The mass distributions have already been shown in Fig. 1 for RHIC and LHC although without the uncorrelated $D\bar{D}$ decays. The p_T and rapidity distributions for lepton pairs with $M = 2, 4,$ and 6 GeV are shown in Fig. 12 for RHIC and 13 for LHC. Here the yield from the uncorrelated $D\bar{D}$ decays are included. The average lepton pair masses for $M > 2$ GeV and transverse momenta at both energies are given in Table 3. The average p_T of the lepton pairs are given for $M > 2$ GeV only for Drell-Yan and thermal dilepton production. The average p_T from heavy quark decays, initial and thermal, are given for all M .

Uncorrelated initial $D\bar{D}$ decays dominate the distributions, by several orders of magnitude at the LHC. However, the like-sign subtraction that removes $\pi^+\pi^-$ and $K\bar{K}$ decays from the continuum should also remove the uncorrelated $D\bar{D}$ decays. The correlated $D\bar{D}$ decays are part of the signal and will not be subtracted. These decays dominate the continuum up to $M = 10$ GeV. At higher masses, the $B\bar{B}$ decays begin to be as important as correlated $D\bar{D}$ decays. The same results are observable in the p_T and rapidity distributions. At RHIC, the contributions from the initial hard processes are above the thermal contributions over all phase space except at $M = 2$ GeV and $y > 4.5$, as seen in Fig. 12(b). The thermal dilepton and thermal charm contributions are somewhat above those of the $B\bar{B}$ and Drell-Yan pairs for $M < 3$ GeV at RHIC. Both thermal contributions have very similar distributions and yields at RHIC energies. The thermal dilepton and thermal $D\bar{D}$ distributions are also similar at the LHC although the thermal charm yield is larger than the thermal lepton pair yield. At the LHC, the $B\bar{B}$ decays produce more lepton pairs than the thermals for $M > 2$ GeV. However, the correlated thermal charm yield is above the $B\bar{B}$ decays at $M = 2$ GeV. The uncorrelated thermal charm yield is larger than

the $B\bar{B}$ decay rate. If all the heavy quark decays could be subtracted, there might be a small window of opportunity to observe thermal dileptons, both prompt and from charm decays, over Drell-Yan production at low p_T , as seen in Fig. 12. Because RHIC is at a significantly lower energy than the LHC, the slopes of the rapidity and p_T distributions of each of the contributions are somewhat different, even in the central region, as seen in Fig. 12. The difference in the slopes could perhaps help disentangle the dilepton sources, if very large rapidities could be measured. All the LHC p_T and rapidity spectra have similar slopes, see Fig. 13, making differentiation more difficult.

Our results suggest that it is very unlikely that the thermal $q\bar{q}$ annihilation signal can be extracted. However, the experimental acceptance has not been included. The acceptance should be smaller for lepton pairs from $D\bar{D}$ decays than for Drell-Yan or thermal dileptons. Since, especially for $D\bar{D}$ decays, large lepton pair mass implies a large rapidity gap, at least one of the $D\bar{D}$ decay leptons may be outside the finite detector acceptance. In particular, relatively few high mass lepton pairs from uncorrelated $D\bar{D}$ decays will be detected, significantly reducing the uncorrelated yield even before like-sign subtraction. The $B\bar{B}$ decay pairs will have a larger acceptance due to the increase in pair p_T over the $D\bar{D} \rightarrow l^+l^-$ decays at the same mass which reduces the rapidity gap. Therefore a judicious choice of kinematic cuts can reduce the initial $D\bar{D}$ acceptance relative to other dilepton sources that produce nearly equal but opposite transverse momentum leptons with $p_T < M$. To show how the finite detector acceptance changes the yield, we choose some realistic cases to examine in more detail.

4.2 RHIC: PHENIX

The RHIC PHENIX detector is specially designed to measure electromagnetic probes. It consists of two central electron arms with a rather small acceptance, $|\eta| \leq 0.35$ and $\pm 30^\circ < \phi < \pm 120^\circ$, one muon arm in the forward direction [54] covering the pseudorapidity region $1.1 \leq \eta \leq 2.4$, and a second muon arm in the backward direction with a similar angular coverage [55]. We assume that electrons with momentum greater than 1 GeV and muons with momentum greater than 2 GeV can be efficiently detected. Although we choose a rather high momentum cut-off, lower momentum leptons will be measured as well. Additional coverage from the electron arms together with the muon arm will partially fill in the rapidity gap between the two detector systems through electron-muon coincidence studies. The rapidity gap between the lepton pairs becomes particularly important when finite acceptance cuts are applied. Pairs with a small rapidity gap are more likely to be accepted, particularly in the central electron arms.

The detector acceptance can have a substantial effect on the relative rates, as shown in Fig. 14 for (a) the central electron arms, (b) the forward muon arm, and (c) the combined $e\mu$ coverage for PHENIX. Note that some of the distributions are limited by statistics. For each system, the accepted lepton pair mass distributions are shown. The percentage of accepted pairs with $M > 2$ GeV and the average lepton pair mass from all our sources in this mass range are given in Table 4. In principle all finite masses are accepted, as suggested from the $H\bar{H}$ decay distributions in Figs. 4-7. However, since the Drell-Yan and thermal dileptons calculations are most reliable for $M > 2$ GeV, we use

$M = 2$ GeV as a lower bound on the accepted masses. Note that many of the $D\bar{D}$ decay pairs, both correlated and uncorrelated, have an invariant mass less than 2 GeV so that the additional mass cut to compare the number of accepted pairs on an equal footing significantly reduces the total acceptance, especially for the uncorrelated $D\bar{D}$ pairs.

The finite acceptance strongly reduces the uncorrelated $D\bar{D}$ production relative to the correlated production, as seen in Fig. 14. In the central detector, $D\bar{D}$ decays have the smallest acceptance due to the relatively large rapidity gap between the leptons. Particularly, the high mass uncorrelated pairs are removed from the spectrum. The $B\bar{B}$ decays have the largest acceptance here because the combination of the relatively small pair rapidity and rapidity gap favors their detection. They will have the largest contribution to the continuum for $M > 6$ GeV, after the correlated $D\bar{D}$ signal is negligible.

In the forward muon arm, the Drell-Yan and $B\bar{B}$ decays have very similar yields for $M > 3$ GeV since the $B\bar{B}$ acceptance will be decreased relative to the tightly correlated Drell-Yan and thermal production with their broader rapidity distributions. Although both correlated and uncorrelated $D\bar{D}$ decays are reduced relative to the smaller rapidity gap of the $B\bar{B}$ decays, the uncorrelated $D\bar{D}$ acceptance is reduced still further because of the larger rapidity gap between the uncorrelated lepton pairs. In general, the broader rapidity coverage in the muon arm increases the acceptance of both the correlated and uncorrelated $D\bar{D}$ pairs. After like-sign subtraction, the initial $D\bar{D}$ decays will dominate the spectrum for most of the pair masses studied.

In Fig. 14(c) we show only the acceptance for correlated and uncorrelated initial $D\bar{D}$ decays to $e\mu$ pairs. The increased rapidity coverage of the combined system results in the acceptance of more low mass uncorrelated $D\bar{D}$ decays. We have not included the yield from any of the other sources since $e\mu$ pairs cannot be produced by correlated Drell-Yan and thermal production. The rate must be large enough for at least two lepton pairs to be produced per event for uncorrelated $e\mu$ pairs to be important (except for $B\bar{B}$ decays) and the yields from the other sources are small enough for such production to be unlikely (see Table 1).

If the uncorrelated $D\bar{D}$ decays can be completely removed by a like-sign subtraction, then $e\mu$ coincidence is a good way to extract the correlated $D\bar{D}$ yield, which constitutes the charm signature. Even with a complete charm measurement, thermal sources will be hard to detect, especially the thermal dileptons. In the muon arm, Drell-Yan and $B\bar{B}$ decays have nearly the same rate and could be hard to separate. However, in the electron arms, for $6 < M < 10$ GeV, $B\bar{B}$ decays are most important and could be removed from the lower mass continuum by a comparison of the slopes. The thermal $D\bar{D}$ signature may be measured below 3 GeV if the initial charm production can be reliably subtracted. At 2 GeV in the central detectors, the accepted thermal $D\bar{D}$ yield is five times larger than the $B\bar{B}$ yield. At low mass and p_T , thermal charm could also be seen in the pair p_T distributions. Measurements from all the detector systems must complement each other for reliable results.

4.3 LHC: ALICE

At the LHC, only one heavy-ion detector, ALICE, is planned. It includes a central detector that will measure dielectrons with $M \leq M_{J/\psi}$ [56] and covering $|\eta| \leq 0.9$. We select leptons with momentum greater than 1 GeV. The ALICE collaboration has also proposed a forward muon spectrometer, with $2.4 \leq \eta \leq 4$ to cover higher mass pairs [57]. We consider only muons with momentum larger than 4 GeV in the muon arm.

The mass distributions for (a) the central detector and (b) the forward muon spectrometer are shown in Fig. 15. The relative rates are similar to the corresponding RHIC detector systems although, overall, the acceptances are larger in the ALICE detector, as shown in Table 5. In the central detector, this is probably due to the full azimuthal coverage and the larger rapidity coverage. While the acceptance cuts substantially reduce the rate from uncorrelated $D\bar{D}$ decays compared to the correlated decays, the uncorrelated yield is still nearly an order of magnitude larger than the correlated yield for masses below 4 GeV. This higher acceptance for uncorrelated pairs means that an accurate like-sign subtraction is crucial. An additional background comes from uncorrelated thermal $D\bar{D}$ decays. In the central detector, the uncorrelated thermal $D\bar{D}$ rate is as large as the initial correlated $D\bar{D}$ rate at low masses. However, in the muon arm, the $B\bar{B}$ decays are clearly the most important source of lepton pairs after the initial charm production due in part to the smaller rapidity gap between the leptons—it is more likely that both decay leptons will lie within the rapidity window of the detector. The acceptance does not decrease in the muon arm because the pair rapidity distribution is not significantly reduced with respect to the Drell-Yan and thermal pair distributions, as is the case at RHIC. The correlated thermal $D\bar{D}$ yield may also be observable at $M \approx 2$ GeV although the $B\bar{B}$ decay rate is within a factor of two here and more difficult to remove reliably. The average mass of the accepted pairs in ALICE are also given in Table 5. The observed trends are similar to the PHENIX results except that the conclusion that the thermal dilepton signal is unlikely to be measured is even stronger here although thermal charm may still be observable.

4.4 Conclusions

Charm production is the dominant source of dileptons in heavy-ion collisions, even with acceptance cuts, for $M < 6 - 8$ GeV. Uncertainties in QCD calculations may change the rates by a factor of two at RHIC and 3-4 at LHC, not enough to affect this conclusion. Charm is both signal and background because the multiple $c\bar{c}$ pair production results in substantial uncorrelated $D\bar{D}$ contributions to the background. We have only included heavy quark production by first collisions. However, multiple hard scattering in AB collisions can increase the charm yield before equilibration.

Nuclear shadowing is not yet well understood for the gluon. If the shadowing effects can be mapped out in phase space, the detection of thermal signals could be improved. Since pA studies are planned at RHIC, nuclear shadowing could be mapped out in phase space. Such measurements are themselves important results. The effects are strongest at the LHC where the saturation of the shadowing curve is reached. Unfortunately this

saturation region is unlikely to be probed at RHIC and no corresponding pA measurements can be performed at the LHC so that the shadowing effects may be more difficult to interpret. It is clear that systematic studies of charm production in pp , pA and AB interactions at the same energy are needed to fully understand charm production.

We stress that our work differs from previous efforts [41, 42] primarily in our estimate of the perturbative background. Kapusta, McLerran and Srivastava [41] assumed hydrodynamic initial conditions similar to ours, but concluded that thermal dileptons dominate the continuum below the Υ . We attribute this striking difference to their estimate of the initial hard scattering processes. First, they omitted the contribution from semileptonic charm decays. They also underestimated the Drell-Yan contribution by using Duke-Owens parton distributions [11], long obsolete. This same Drell-Yan estimate was also used in the comparison with dilepton production by the parton cascade model [42].

Our calculations show that charm cannot be omitted. The production of charm-decay and Drell-Yan dileptons in primary collisions in any parton cascade or hydrodynamic model must agree with perturbative QCD and, therefore, the rates should be similar to ours. Other initial charm calculations [52] are within a factor of two to three of ours, within the theoretical uncertainties involving the quark mass and scale. The $c\bar{c}$ production rate in the parton cascade model agrees with perturbative QCD in pp collisions but overestimates the importance of flavor excitation [14], leading to a larger charm yield than ours, particularly at RHIC [31]. However, we have omitted cascading of the c and \bar{c} quarks in the high density medium, which can lead to energy loss [58] (similar to ‘jet quenching’ [59]). If this loss is sufficient, these quarks can be equilibrated with the flowing plasma. Since it is highly unlikely that all of the $c\bar{c}$ pairs can annihilate, cascading will not change the number of pairs appreciably.

We expect that thermal charm will prove to be an experimentally accessible temperature probe at RHIC and LHC. On the other hand, we emphasize that thermal $q\bar{q}$ annihilation, perhaps the more familiar thermal signal, will be much more difficult to pick out. Thermal annihilation would be a more direct thermometer because the kinematics of the lepton pair specifies the off-shell photon’s four momentum. However, the heavy quark and Drell-Yan contributions are too high for the steeply-falling thermal contributions to be extracted, unless the charm contributions can be reliably subtracted.

What is the best way to measure charm? Coincidence measurements of $e\mu$ can prove useful. Charm was first measured by this method at the ISR [60] and such coincidence measurements are planned for PHENIX [54]. Pairs of like-sign electrons may also offer a measure of uncorrelated charm production. Charm was measured with single electrons by a study of the e/π ratio at the ISR [61]. Additionally, semileptonic decays can be experimentally tagged and separated from direct production of lepton pairs with a vertex detector. If a detached vertex is observed for at least one of the leptons, then direct production of the pair can be ruled out. Such a vertex detector is planned for the STAR detector [62] at RHIC. Another technique for reducing the signal levels from semileptonic decays is the use of selective kinematic cuts. Since the leptons from decays have a weaker correlation in rapidity or angle than those from directly produced pairs, cuts can be placed on these variables. While some signal events will be lost, the signal to background ratio

can be improved for large acceptance detectors.

SG, PVR, and RV thank the Institute for Nuclear Theory at the University of Washington in Seattle for their hospitality. RV thanks Brookhaven National Laboratory and the University of Jyväskylä for their hospitality. We are grateful to J. Carroll, K. Geiger, W. M. Geist, B. Jacak, D. Jouan, V. Koch, J. Smith and E. V. Shuryak for discussions and K. J. Eskola for providing the shadowing parameterizations used in the paper.

A Appendix: Shadowing Effects on Initial Processes

When the charged parton distributions are probed in deep-inelastic scattering with a nuclear target and compared to a deuterium target, the ratio $R_{F_2} = F_2^A/F_2^D$ has a characteristic shape as a function of x . The low x region, below $x \sim 0.1$, is referred to as the shadowing region, and between $x \sim 0.3$ and 0.7 is the EMC region. In both regions a depletion is observed in the heavy nucleus relative to deuterium. At very low x , R_{F_2} appears to saturate [63]. Between the shadowing and EMC regions, an enhancement occurs, called antishadowing, where $R_{F_2} > 1$. There is also an enhancement as $x \rightarrow 1$, assumed to be due to Fermi motion of the nucleons. The entire nuclear dependence is often referred to as shadowing. Although the behavior of R_{F_2} is not well understood, the effect has been described by either an interplay of coherent and incoherent multiple scatterings in the target or a modification of the parton densities in nuclear matter. In any case, the effect can be modeled by an A dependent fit to the nuclear deep-inelastic scattering data and implemented by a modification of the parton distributions in the proton. In this appendix, we show the effect of two different parameterizations of the nuclear parton densities to illustrate how the Drell-Yan and $Q\bar{Q}$ distributions calculated for pp interactions might change in nuclear collisions at RHIC and LHC.

In the central region at RHIC and LHC, the values of x probed are small enough for the hard processes we consider to be predominantly in the shadowing region. However, the momentum fractions increase with pair mass, transverse momentum, and rapidity. At $y = 0$ and $p_T = 0$, $x \sim M/\sqrt{s}$ so that in the mass range $2 < M < 6$ GeV, $0.01 < x < 0.03$ at RHIC and $3.6 \times 10^{-4} < x < 1.09 \times 10^{-3}$ at the LHC. It follows that R_{F_2} may change significantly at RHIC. At the LHC, x is small enough for the shadowing to be saturated over most measurable rapidities. The most important point to note is that the reduction in the Au+Au cross section is never significantly more than a factor of two for any of the processes considered. If the shadowing function can be mapped out in pA interactions at RHIC, as discussed in Ref. [4], then the corrections to AA interactions may be relatively clear for $Q\bar{Q}$ and Drell-Yan production, especially since the lepton pairs from $Q\bar{Q}$ decays should reflect the shape of the shadowing function in the same way as the $Q\bar{Q}$ pairs themselves [4].

The first parameterization is a general fit to the most recent nuclear deep-inelastic scattering data. The fit does not differentiate between quark, antiquark, and gluon modifications and does not include evolution in Q^2 . It is not designed to satisfy the baryon

number or momentum sum rules. The functional form of R_{F_2} is [15]

$$R_{F_2} = \begin{cases} R_s \frac{1 + 0.0134(1/x - 1/x_{\text{sh}})}{1 + 0.0127A^{0.1}(1/x - 1/x_{\text{sh}})} & x < x_{\text{sh}} \\ a_{\text{emc}} - b_{\text{emc}}x & x_{\text{sh}} < x < x_{\text{fermi}} \\ R_f \left(\frac{1 - x_{\text{fermi}}}{1 - x} \right)^{0.321} & x_{\text{fermi}} < x < 1 \end{cases}, \quad (1)$$

where $R_s = a_{\text{emc}} - b_{\text{emc}}x_{\text{sh}}$, $R_f = a_{\text{emc}} - b_{\text{emc}}x_{\text{fermi}}$, $b_{\text{emc}} = 0.525(1 - A^{-1/3} - 1.145A^{-2/3} + 0.93A^{-1} + 0.88A^{-4/3} - 0.59A^{-5/3})$, and $a_{\text{emc}} = 1 + b_{\text{emc}}x_{\text{emc}}$. The fit fixes $x_{\text{sh}} = 0.15$, $x_{\text{emc}} = 0.275$ and $x_{\text{fermi}} = 0.742$. In Fig. 16(a) we show $R_{F_2}(x)$ for $A = 197$. In the nucleus, the parton densities are modified so that

$$q_f^A(x, \mu) = R_{F_2}(x)q_f^p(x, \mu) \quad (2)$$

$$g^A(x, \mu) = R_{F_2}(x)g^p(x, \mu), \quad (3)$$

where q_f represents both valence and sea quarks. Since $R_{F_2}(x)$ is scale independent and the parton densities are treated equivalently, the ratio of hard process production in Au+Au to pp collisions at the same energy is

$$R(y, p_T, M) = \frac{d\sigma_{\text{AuAu}}/dydp_TdM}{d\sigma_{pp}/dydp_TdM} \propto R_{F_2}(x_1)R_{F_2}(x_2). \quad (4)$$

In Fig. 16(b)-(d) and Fig. 17 we show the nuclear effect on leading order calculations of heavy quark and Drell-Yan production. Figures 16(b)-(d) show $R(p_T)$ for single c and b mesons and $R(M)$ and $R(y)$ for $D\bar{D}$ and $B\bar{B}$ pairs at RHIC and LHC. At RHIC energies, the increase of R with p_T and M reflects the integration over the low x_1, x_2 midrapidity contributions as well as the growth of R_{F_2} as x approaches the antishadowing region, reached at $M \simeq 20$ GeV for $D\bar{D}$ and $B\bar{B}$ pairs. Note that $R(M)$ is almost identical for $D\bar{D}$ and $B\bar{B}$ production, as it should be since at fixed M the same x values are probed. The B p_T ratios are generally flatter because the change in $R_{F_2}(x)$ with p_T is slower than the change in $R_{F_2}(x)$ for D production at the same energy. The ratio $R(y)$ is nearly constant for $D\bar{D}$ production at RHIC, caused by the coincidence of x_1 increasing toward the antishadowing region while x_2 decreases into the saturation region. In contrast, the $B\bar{B}$ ratio decreases with rapidity at RHIC since at $y = 2$, x_1 lies in the EMC region while $x_2 \sim 0.001$. Figure 17 shows $R(y)$ and $R(M)$ for Drell-Yan pairs at RHIC and LHC. At RHIC $R(y)$ increases with mass at $y = 0$ due to the increase of R_{F_2} as $x_1 = x_2$ grows from 0.01 to 0.03. At higher rapidities, $R_{F_2}(x_2)$ moves toward the saturation region while $R_{F_2}(x_1)$ passes through the EMC region and then rises again as $x_1 \rightarrow 1$. Near the edge of phase space, the transition from the EMC region to the Fermi motion region can be seen. The phase space is depleted at higher rapidities for lower masses. At the LHC x_1 remains in the shadowing region for $y < 4$. The ratios of rapidity integrated mass distributions rise slowly with mass, reflecting the broad rapidity distributions.

The second parameterization modifies the valence and sea quark and gluon distributions separately and includes evolution with the square of the momentum transfer, Q^2 , [16] but is based on an older fit to the data using the Duke-Owens parton densities [11].

The exact form of $R_{F_2}(x, Q_0)$ is given in Ref. [16]. The initial scale is chosen to be $Q_0 = 2$ GeV and the Q^2 evolution is done with both the standard Altarelli-Parisi evolution and with gluon recombination at high density. The gluon recombination terms do not strongly alter the evolution. In this case, the nuclear parton densities are modified so that

$$q_V^A(x, \mu) = R_V(x, \mu)q_V^p(x, \mu) \quad (5)$$

$$q_S^A(x, \mu) = R_S(x, \mu)q_S^p(x, \mu) \quad (6)$$

$$g^A(x, \mu) = R_G(x, \mu)g^p(x, \mu) , \quad (7)$$

where $q_V = u_v + d_v$ is the valence quark density and $q_S = 2(\bar{u} + \bar{d} + \bar{s})$ is the total sea quark density and we assume that R_V and R_S affect the individual valence and sea quarks identically. The ratios were constrained in the model [16] by assuming that $R_{F_2} \approx R_V$ at large x and $R_{F_2} \approx R_S$ at small x since $xq_V(x, \mu) \rightarrow 0$ as $x \rightarrow 0$. We use ansatz 1 for the gluons, $R_{F_2} \approx R_G$ for all x [16], since one might expect more shadowing for the sea quarks, generated from gluons, at small x . The parton densities satisfy baryon number conservation $\int_0^1 dx q_V^{p,A}(x, \mu) = 3$ and momentum conservation $\int_0^1 dx x(q_V^{p,A}(x, \mu) + q_S^{p,A}(x, \mu) + g^{p,A}(x, \mu)) = 1$ at all μ . We have used the MRS D-' densities with this parameterization instead of the original parton densities, leading to some small deviations in the momentum sum but the general trend is unchanged.

Figure 18(a) shows the ratios R_V (solid curves), R_S (dashed curves), and R_G (dot-dashed curves) for the minimum, Q_0 , and maximum, 10 GeV, values of Q for $A = 200$. Outside this range the ratios are fixed to those at 10 GeV. The valence quarks show little Q^2 evolution, the gluons the greatest. The sea quarks evolve more slowly than the gluons and, at $Q = 10$ GeV, $R_S \approx R_{F_2}$ of the first parameterization, eq. (1). The ratios of AA to pp production of $Q\bar{Q}$ and Drell-Yan pairs are shown in Fig. 18(b)-(d) and Fig. 19. The ratio R for this parameterization is not as straightforward to write down as in eq. (4) except for gg fusion. For example for $q\bar{q} \rightarrow Q\bar{Q}$,

$$R \propto \frac{R_S(x_1)R_S(x_2)\sum_{q=u,d,s}2q_s(x_1)\bar{q}_s(x_2) + [R_V(x_1)R_S(x_2)\sum_{q=u,d}q_v(x_1)\bar{q}_s(x_2) + (1 \rightarrow 2)]}{\sum_{q=u,d,s}2q_s(x_1)\bar{q}_s(x_2) + [\sum_{q=u,d}q_v(x_1)\bar{q}_s(x_2) + (1 \rightarrow 2)]} , \quad (8)$$

where q_s is a generic sea quark distribution and the μ dependence has been suppressed. The fast evolution of the gluons has the strongest effect on the charm and bottom production since $Q\bar{Q}$ production by gluons is dominant. In fact, for $b\bar{b}$ production at RHIC energies, the shadowing effect has nearly vanished in $R(p_T)$. The ratios for Au+Au to pp are shown in Fig. 18(b)-(d) as a function of quark p_T and pair mass and rapidity. The trends are the same as for the first parameterization but, overall, the $Q\bar{Q}$ distributions are not as strongly modified since the effect decreases for increasing p_T and M . As seen in a comparison of Fig. 19 with Fig. 17, the shadowing effect is actually stronger for low mass Drell-Yan production with this parameterization due to the strong sea quark shadowing at Q_0 .

In either case, the reduction in AA yield relative to pp due to shadowing is generally not larger than a factor of two, depending on the shadowing model. It is important to note that the total depletion is a dependent on both x and Q and is not a constant factor as a function of p_T , M and y in either model.

References

- [1] R. Vogt, B.V. Jacak, P.L. McGaughey and P.V. Ruuskanen, Phys. Rev. **D49** (1994) 3345.
- [2] S. Gavin *et al.*, Int. J. Mod. Phys. **A10** (1995) 2961.
- [3] P.L. McGaughey *et al.*, Int. J. Mod. Phys. **A10** (1995) 2999.
- [4] Z. Lin and M. Gyulassy, Columbia University preprint 1995, CU-TP 714.
- [5] H.G. Fischer and W.M. Geist, Z. Phys. **C19** (1983) 159.
- [6] M.L. Mangano, P. Nason, and G. Ridolfi, Nucl. Phys. **B373** (1992) 295.
- [7] P. Arnold and R. Kauffman, Nucl. Phys. **B349** (1991) 381.
- [8] A.D. Martin, W.J. Stirling and R.G. Roberts, Phys. Lett. **306B**, 145 (1993).
- [9] H. Plochow-Besch, Comp. Phys. Comm. **75**, (1993) 396.
- [10] M. Derrick *et al.*, ZEUS Collab., Phys. Lett. **B316** (1993) 515.
- [11] D.W. Duke and J.F. Owens, Phys. Rev. **D30** (1984) 49.
- [12] A.D. Martin, W.J. Stirling and R.G. Roberts, Phys. Lett. **B354** (1995) 155.
- [13] M.R. Adams *et al.*, E665 Collab., Fermilab preprint FNAL Pub-95/396-E.
- [14] R.K. Ellis, in *Physics at the 100 GeV Scale*, Proceedings of the 17th SLAC Summer Institute, Stanford, California, 1989, edited by E.C. Brennan (SLAC Report No. 361, Stanford, 1990).
- [15] K.J. Eskola, J. Qiu, and J. Czyzewski, private communication.
- [16] K.J. Eskola, Nucl. Phys. **B400** (1993) 240.
- [17] P.J. Rijken and W.L. van Neerven, Phys. Rev. **D51** (1995) 44.
- [18] R. Vogt, S.J. Brodsky, and P. Hoyer, Nucl. Phys. **B383** (1992).
- [19] S. Banerjee and S.N. Ganguli, Phys. Rev. **D33** (1986) 1278.
- [20] P. Nason, S. Dawson, and R.K. Ellis, Nucl. Phys. **B303** (1988) 607.
- [21] P. Nason, S. Dawson, and R.K. Ellis, Nucl. Phys. **B327** (1989) 49.
- [22] W. Beenakker, H. Kuijf, W.L. van Neerven, and J. Smith, Phys. Rev. **D40** (1989) 54; W. Beenakker, W.L. van Neerven, R. Meng, G.A. Schuler, and J. Smith, Nucl. Phys. **B351** (1991) 507.

- [23] S.P.K. Tavernier, Rep. Prog. Phys. **50** (1987) 1439. This review contains references to all data prior to 1988, including the ISR measurements.
- [24] M.L. Mangano, P. Nason, and G. Ridolfi, Nucl. Phys. **B405** (1993) 507.
- [25] G.A. Alves *et al.*, E769 Collab., Phys. Rev. Lett. **70** (1993) 722.
- [26] M.J. Leitch *et al.*, E789 Collab., Phys. Rev. Lett. **72** (1994) 2542.
- [27] J.A. Appel, Ann. Rev. Nucl. Part. Sci. **42** (1992) 367.
- [28] M. Glück, E. Reya and A. Vogt, Z. Phys. **C53** (1992) 127.
- [29] R. Vogt, LBL-37105, to be published in Z. Phys. **C**.
- [30] I. Sarcevic and P. Valerio, Phys. Lett. **B338** (1994) 426; Phys. Rev. **C51** (1995) 1433.
- [31] K. Geiger, Phys. Rev. **D47** (1993) 133.
- [32] R.M. Baltrusaitis *et al.*, Mark-III Collab., Phys. Rev. Lett. **54** (1985) 1976.
- [33] S. Behrends *et al.*, CLEO Collab., Phys. Rev. Lett. **59** (1987) 407.
- [34] M. Aguilar-Benitez *et al.*, Particle Data Group, Phys. Rev. **D50** (1994) 1173.
- [35] K. Kajantie, R. Raitio, and P.V. Ruuskanen, Nucl. Phys. **B222** (1983) 152.
- [36] M. Kataja, Z. Phys. **C38** (1988) 419.
- [37] K. Kajantie and P.V. Ruuskanen, Z. Phys. **C44** (1989) 167.
- [38] M.I. Gorenstein and O.P. Pavlenko, Z. Phys. **C37** (1988) 611.
- [39] C. Gale and P. Lichard, Phys. Rev. **D49** (1994) 3338.
- [40] A.V. Leonidov and P.V. Ruuskanen, Heavy Ion Physics, **1** (1995) 61.
- [41] J.I. Kapusta, L. McLerran, and D.K. Srivastava, Phys. Lett. **B283** (1992) 145.
- [42] K. Geiger and J.I. Kapusta, Phys. Rev. Lett. **70** (1993) 1920.
- [43] D. Seibert and T. Altherr, Phys. Rev. **D48** (1993) 3386.
- [44] F. Karsch, Nucl. Phys. **A590** (1995) 367c.
- [45] K.J. Eskola, Nucl. Phys. **A590** (1995) 383c.
- [46] K.J. Eskola, K. Kajantie and P.V. Ruuskanen, Phys. Lett. **B332** (1994) 191.
- [47] P.V. Ruuskanen, Z. Phys. **C38** (1988) 219.
- [48] M. Kataja, J. Letessier, P.V. Ruuskanen, and A. Tounsi, Z. Phys. **C55** (1992) 153.

- [49] E.V. Shuryak, Phys. Rev. Lett. **68** (1992) 3270.
- [50] A. Shor, Phys. Lett. **B215** (1988) 375. A. Shor, Phys. Lett. **B 233** (1989) 231.
- [51] B. L. Combridge, Nucl. Phys. **B151** (1979) 429.
- [52] P. Levai, B. Müller, and X.-N. Wang, Phys. Rev. **C51** (1995) 3326.
- [53] Z. Lin and M. Gyulassy, Phys. Rev. **C51** (1995) 2177.
- [54] PHENIX Conceptual Design Report, 1993 (unpublished).
- [55] PHENIX/Spin Collaboration Report, 1995 (unpublished).
- [56] ALICE Letter of Intent, CERN Report No. CERN/LHCC/93-16, 1993 (unpublished).
- [57] ALICE Report, CERN/LHCC/95-24, 1995 (unpublished).
- [58] S. Gavin and J. Milana, Phys. Rev. Lett. **68** (1992) 1834.
- [59] M. Gyulassy, in “Nuclei at HERA and Heavy-Ion Physics”, proceedings of the workshop at Brookhaven National Laboratory, 17-18 Nov. 1995, S. Gavin and M. Strickman eds.
- [60] A.G. Clark *et al.*, Phys. Lett. **77B** (1978) 339. A. Chilingarov *et al.*, Phys. Lett. **B83** (1979) 136.
- [61] M. Tannenbaum, private communication; Nucl. Phys. **B113** (1976) 189.
- [62] STAR Conceptual Design Report, LBL PUB-5347, 1992.
- [63] M.R. Adams *et al.*, Phys. Rev. Lett. **68** (1992) 3266.

Source	N_l		
	$M_l = 2$ GeV	$M_l = 4$ GeV	$M_l = 6$ GeV
DD_{uncorr}	1.94×10^{-1}	4.5×10^{-2}	1.67×10^{-2}
DD_{corr}	2.31×10^{-2}	2.10×10^{-3}	3.10×10^{-4}
BB	1.38×10^{-4}	6.85×10^{-5}	2.52×10^{-5}
DY	5.29×10^{-4}	3.86×10^{-5}	8.06×10^{-6}
$l^+l^-_{\text{th}}$	9.07×10^{-4}	7.6×10^{-6}	1.4×10^{-7}
DD_{th}	9.29×10^{-4}	5.18×10^{-6}	—

Table 1: Number of lepton pairs per event from each of our sources in central Au+Au collisions at RHIC.

Source	N_{ll}		
	$M_{ll} = 2 \text{ GeV}$	$M_{ll} = 4 \text{ GeV}$	$M_{ll} = 6 \text{ GeV}$
$\overline{DD}_{\text{uncorr}}$	4.80×10^2	1.90×10^2	1.07×10^2
$\overline{DD}_{\text{corr}}$	1.40×10^0	1.69×10^{-1}	2.95×10^{-2}
\overline{BB}	2.05×10^{-2}	1.15×10^{-2}	4.98×10^{-3}
DY	6.90×10^{-3}	7.83×10^{-4}	2.06×10^{-4}
$l^+ l_{\text{th}}^-$	1.43×10^{-2}	4.68×10^{-4}	3.26×10^{-5}
$\overline{DD}_{\text{th,corr}}$	4.8×10^{-2}	1.02×10^{-3}	3.57×10^{-5}
$\overline{DD}_{\text{th,uncorr}}$	1.42×10^0	4.32×10^{-1}	2.03×10^{-1}

Table 2: Number of lepton pairs per event from each of our sources in central Pb+Pb collisions at LHC.

\sqrt{s}	200 GeV		5.5 TeV	
Source	$\langle M_{ll} \rangle$ (GeV)	$\langle p_{T, ll} \rangle$ (GeV)	$\langle M_{ll} \rangle$ (GeV)	$\langle p_{T, ll} \rangle$ (GeV)
DD_{uncorr}	3.73	0.84	4.57	1.00
DD_{corr}	2.41	0.77	3.03	0.84
BB	3.95	1.91	4.20	2.05
DY	2.45	1.68	2.68	2.45
$l^+l^-_{\text{th}}$	2.44	1.06	2.61	1.26
$DD_{\text{th,corr}}$	2.39	0.85	2.52	0.98
$DD_{\text{th,uncorr}}$	-	-	2.28	0.97

Table 3: Average lepton pair mass (for $M_{ll} > 2$ GeV) and transverse momentum at RHIC and LHC. For the Drell-Yan and thermal lepton pairs, the average p_T 's are calculated for $M_{ll} > 2$ GeV only while all the average p_T 's from heavy quark decays are for all masses.

Source	e^+e^-		$\mu^+\mu^-$		$e^\pm\mu^\mp$	
	% Acc.	$\langle M_{ee} \rangle$ (GeV)	% Acc.	$\langle M_{\mu\mu} \rangle$ (GeV)	% Acc.	$\langle M_{e\mu} \rangle$ (GeV)
DD_{uncorr}	0.01	2.75	0.07	2.53	0.084	3.2
DD_{corr}	0.032	3.05	0.42	2.84	0.08	3.74
BB	0.60	4.53	1.7	3.56	-	-
DY	0.16	3.15	3.7	2.64	-	-
$l^+l^-_{\text{th}}$	0.23	2.51	3.3	2.18	-	-
DD_{th}	0.014	2.47	0.12	2.58	-	-

Table 4: Percentage of lepton pairs with $M_{ll} > 2$ GeV accepted in the PHENIX detector and their average pair mass. We have included the central electron arms, the forward muon arm, and a combination of electrons and muons from both detectors.

	e^+e^-		$\mu^+\mu^-$	
	% Acc.	$\langle M_{ee} \rangle$ (GeV)	% Acc.	$\langle M_{\mu\mu} \rangle$ (GeV)
DD_{uncorr}	0.093	2.69	0.12	2.58
DD_{corr}	0.44	3.10	0.67	2.92
$B\bar{B}$	4.42	4.33	3.58	4.01
DY	3.6	2.62	5.27	2.58
$l^+l^-_{\text{th}}$	4.9	2.55	4.76	2.22
$DD_{\text{th,corr}}$	0.46	2.52	0.29	2.34
$DD_{\text{th,uncorr}}$	0.33	2.70	0.056	2.49

Table 5: Percentage of lepton pairs with $M_{ll} > 2$ GeV accepted in the ALICE detector and their average pair mass. We have included the central detector and the proposed forward muon arm.

Figure Captions

Figure 1. The lepton pair mass distributions are given in (a) for central Au+Au collisions at RHIC and (b) for central Pb+Pb collisions at LHC. The contributions are: Drell-Yan (dashed) and thermal dilepton (dot-dashed-dashed) production and thermal $D\bar{D}$ decays (dotted), as well as initial correlated (dot-dashed) $D\bar{D}$ and $B\bar{B}$ (dot-dot-dashed) production and decay. Note that lepton pairs from uncorrelated initial $D\bar{D}$ decays (as well as uncorrelated thermal $D\bar{D}$ decays at the LHC) have not been included here but are a very large contribution to the continuum.

Figure 2. The NLO Drell-Yan pair production rate in central Au+Au collisions at $\sqrt{s} = 200$ GeV. The pair p_T (a), mass (b), and rapidity (c) distributions are shown. The p_T distributions are given at $y = 0$ (solid) and $y = 2$ (dashed) for $M = 2, 4,$ and 6 GeV (the upper, middle, and lower sets of curves respectively). In (c) the rapidity distributions are calculated for $M = 2$ GeV (solid), 4 GeV (dashed), and 6 GeV (dot-dashed).

Figure 3. The same as Fig. 2 for central Pb+Pb collisions at $\sqrt{s} = 5.5$ TeV.

Figure 4. The rate of initial $c\bar{c}$ (solid) and $D\bar{D}$ (dashed) pair production to NLO in central Au+Au collisions at $\sqrt{s} = 200$ GeV. The pair p_T (a), mass (b), rapidity gap (c), and pair rapidity (d) distributions are shown. Additionally, the lepton pair p_T , mass, and rapidity distributions from correlated (dot-dashed) and uncorrelated (dotted) $D\bar{D}$ pair decays are shown for central Au+Au collisions.

Figure 5. The same as Fig. 4 for central Pb+Pb collisions at $\sqrt{s} = 5.5$ TeV.

Figure 6. The same as Fig. 4 for the $b\bar{b}$ and $B\bar{B}$ production rate to NLO in central Au+Au collisions at $\sqrt{s} = 200$ GeV.

Figure 7. The same as Fig. 6 for central Pb+Pb collisions at $\sqrt{s} = 5.5$ TeV.

Figure 8. The thermal lepton pair rate in central Au+Au collisions for $M \geq 2$ GeV and $\sqrt{s} = 200$ GeV. The lepton pair p_T (a), mass (b), rapidity gap (c), and rapidity (d) distributions are shown. The p_T , rapidity gap, and rapidity distributions are given for $M = 2$ (solid), 4 (dashed), and 6 (dot-dashed) GeV.

Figure 9. The same as Fig. 8 for central Pb+Pb collisions at $\sqrt{s} = 5.5$ TeV.

Figure 10. The thermal $c\bar{c}$ (solid) and $D\bar{D}$ (dashed) pair production rate in central Au+Au collisions at $\sqrt{s} = 200$ GeV. The pair p_T (a), mass (b), rapidity gap (c), and rapidity (d) distributions are given. The lepton pairs from thermal $D\bar{D}$ decays are shown in the dot-dashed curves.

Figure 11. The same as Fig. 10 for central Pb+Pb collisions at $\sqrt{s} = 5.5$ TeV. Uncorrelated thermal $D\bar{D}$ decays are also included (dotted curves).

Figure 12. The contributions to the dilepton spectrum in central Au+Au collisions at $\sqrt{s} = 200$ GeV for pairs with $M = 2, 4,$ and 6 GeV. The p_T distributions are given in (a), (c), and (e) while the pair rapidity distributions are shown in (b), (d), and (f). The distributions from Drell-Yan (dashed) and thermal dilepton (solid) production and thermal $D\bar{D}$ decays (dotted), the initial correlated (dot-dashed) and uncorrelated (dot-dashed-dashed) $D\bar{D}$ and $B\bar{B}$ (dot-dot-dashed) production and decay are included.

Figure 13. The same as Fig. 12 for central Pb+Pb collisions at $\sqrt{s} = 5.5$ TeV. In addition to the contributions shown in Fig. 12, uncorrelated thermal $D\bar{D}$ decays are shown in the dot-dot-dashed-dashed curves.

Figure 14. The mass distributions of pairs accepted into the PHENIX detector in central Au+Au collisions at RHIC. The acceptance cuts are shown for pairs in (a) the central electron detector, (b) the forward muon arm, and (c) pairs formed when an electron is accepted into one of the PHENIX central arms and an opposite sign muon is accepted into the forward arm. The contributions are: Drell-Yan (dashed) and thermal dilepton (solid) production and thermal $D\bar{D}$ (dotted), initial correlated (dot-dashed) and uncorrelated (dot-dashed-dashed) $D\bar{D}$, and initial $B\bar{B}$ (dot-dot-dashed) production and decay. In (c), only the mass distributions for correlated and uncorrelated $D\bar{D} \rightarrow e^\pm \mu^\mp X$ decays are shown.

Figure 15. The same as Fig. 14 for pairs accepted into the ALICE detector in central Pb+Pb collisions at LHC. The accepted distributions are given for (a) the central detector and (b) the proposed forward muon arm. In addition to the contributions shown in Fig. 14, uncorrelated thermal $D\bar{D}$ decays are shown in the dot-dot-dashed-dashed curves.

Figure 16. (a) The shadowing function $R_{F_2}(x)$ for $A = 197$. We also show the charm and bottom Au+Au to pp production ratios as a function of (b) heavy quark p_T , (c) $Q\bar{Q}$ invariant mass and (d) $Q\bar{Q}$ pair rapidity. Charm production is given in the solid curve at RHIC and the dashed curve at LHC. Bottom production is shown in the dot-dashed curve for RHIC and the dotted curve for LHC. Both Au+Au and pp production is calculated at $\sqrt{s} = 200$ GeV for RHIC and $\sqrt{s} = 5.5$ TeV at the LHC.

Figure 17. The ratio of Drell-Yan rapidity and mass distributions in Au+Au to pp collisions at $\sqrt{s} = 200$ GeV at RHIC and 5.5 TeV at the LHC. The ratio $R(y)$ is given for $M=2$ (solid), 4 (dashed) and 6 (dot-dashed) GeV for RHIC (a) and LHC (c). The mass $R(M)$ is also given for RHIC (b) and LHC (d).

Figure 18. (a) The shadowing functions $R_V(x)$ (solid), $R_S(x)$ (dashed) and $R_g(x)$ (dot-dashed) for $Q = 2$ (lower curves) and 10 GeV (upper curves) for $A = 200$. We also show the charm and bottom Au+Au to pp production ratios as in Fig. 16 but with the

shadowing functions given in (a).

Figure 19. The same as in Fig. 17 with the shadowing functions as in Fig. 18(a).

Figure 1

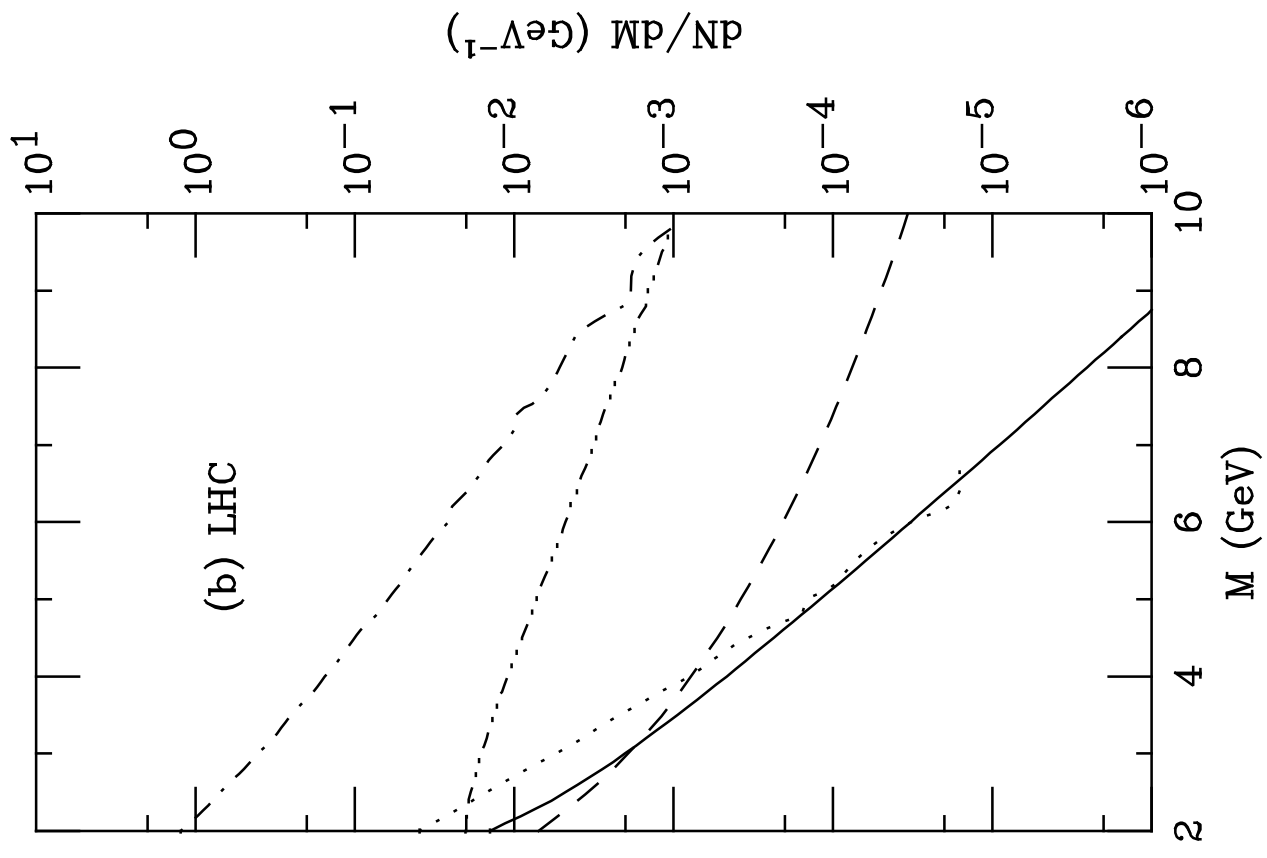
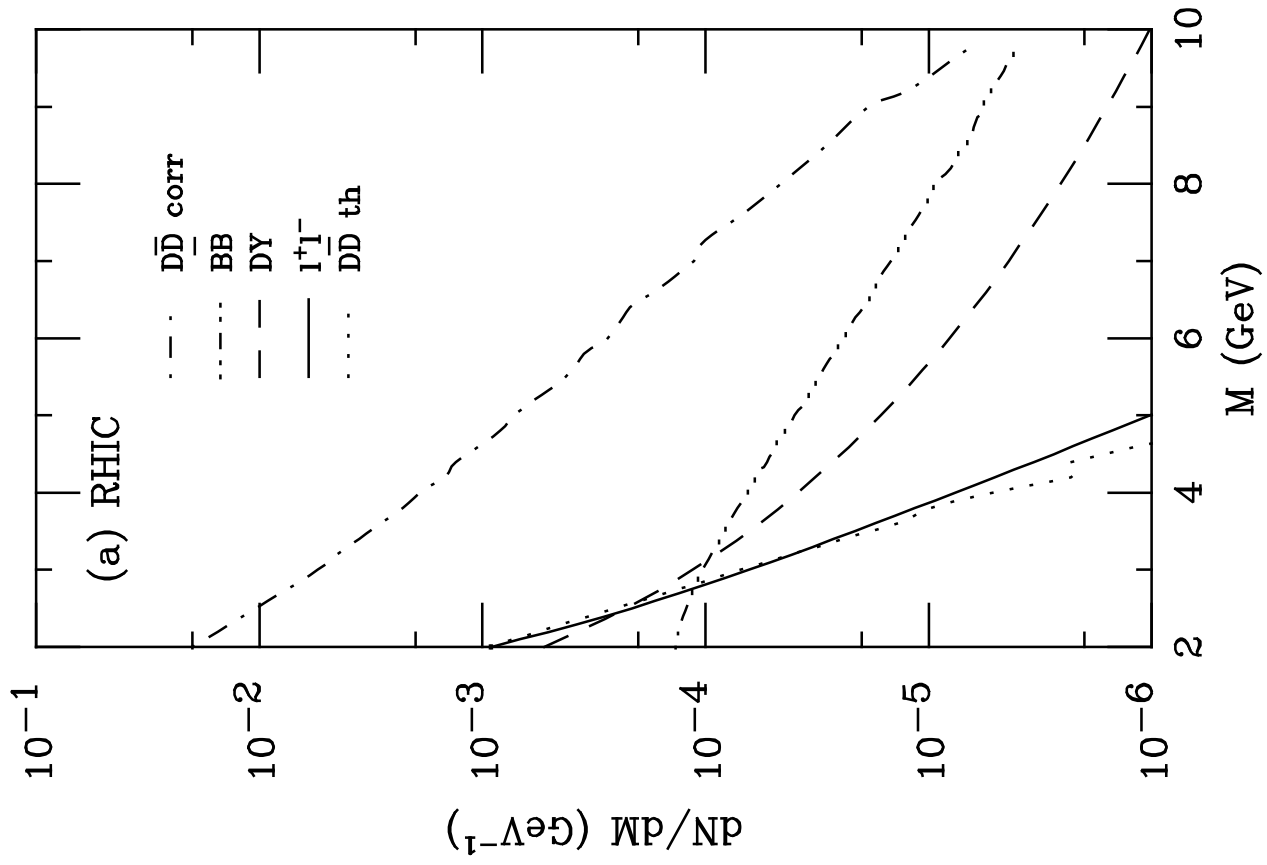


Figure 2

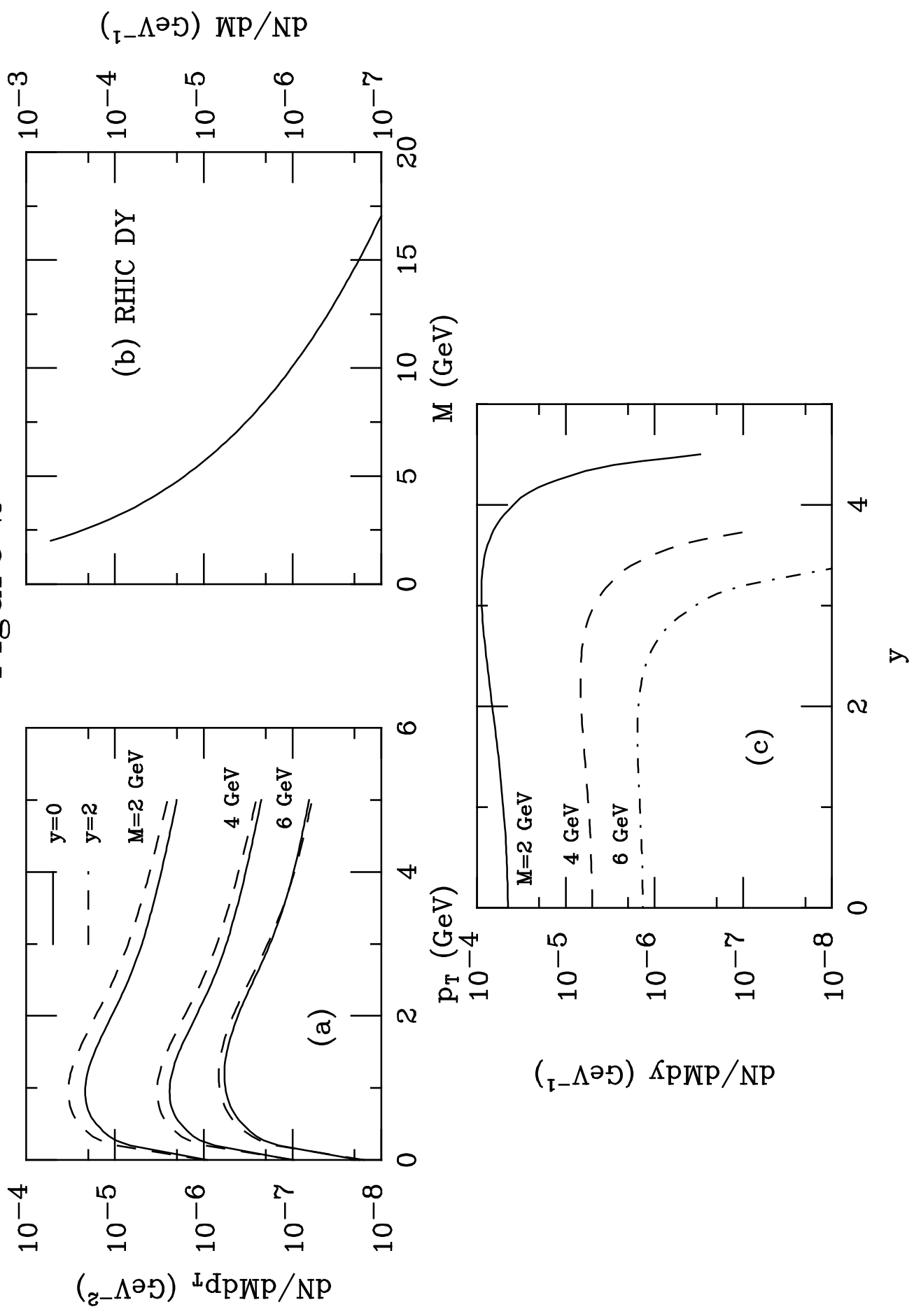


Figure 3

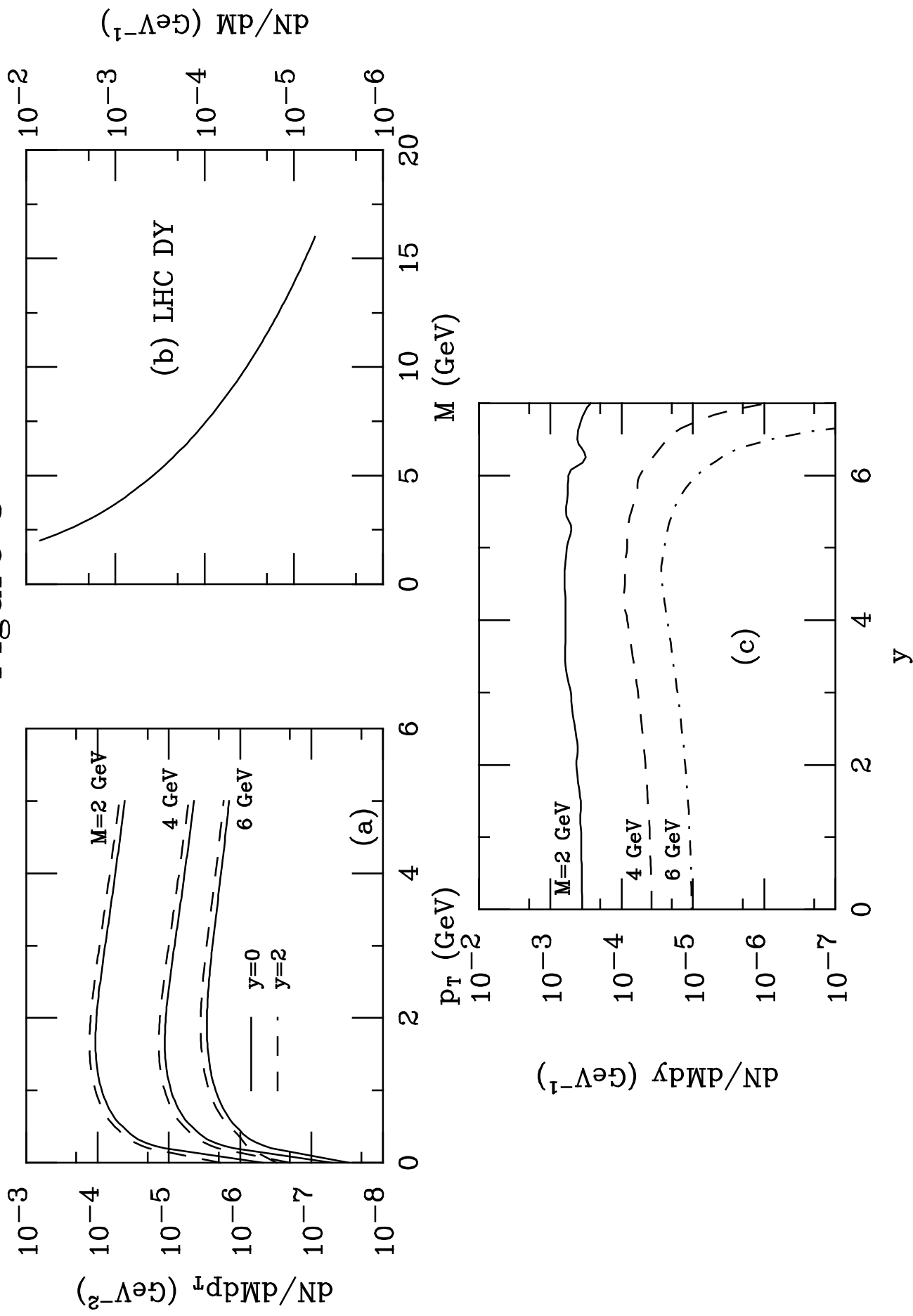


Figure 4

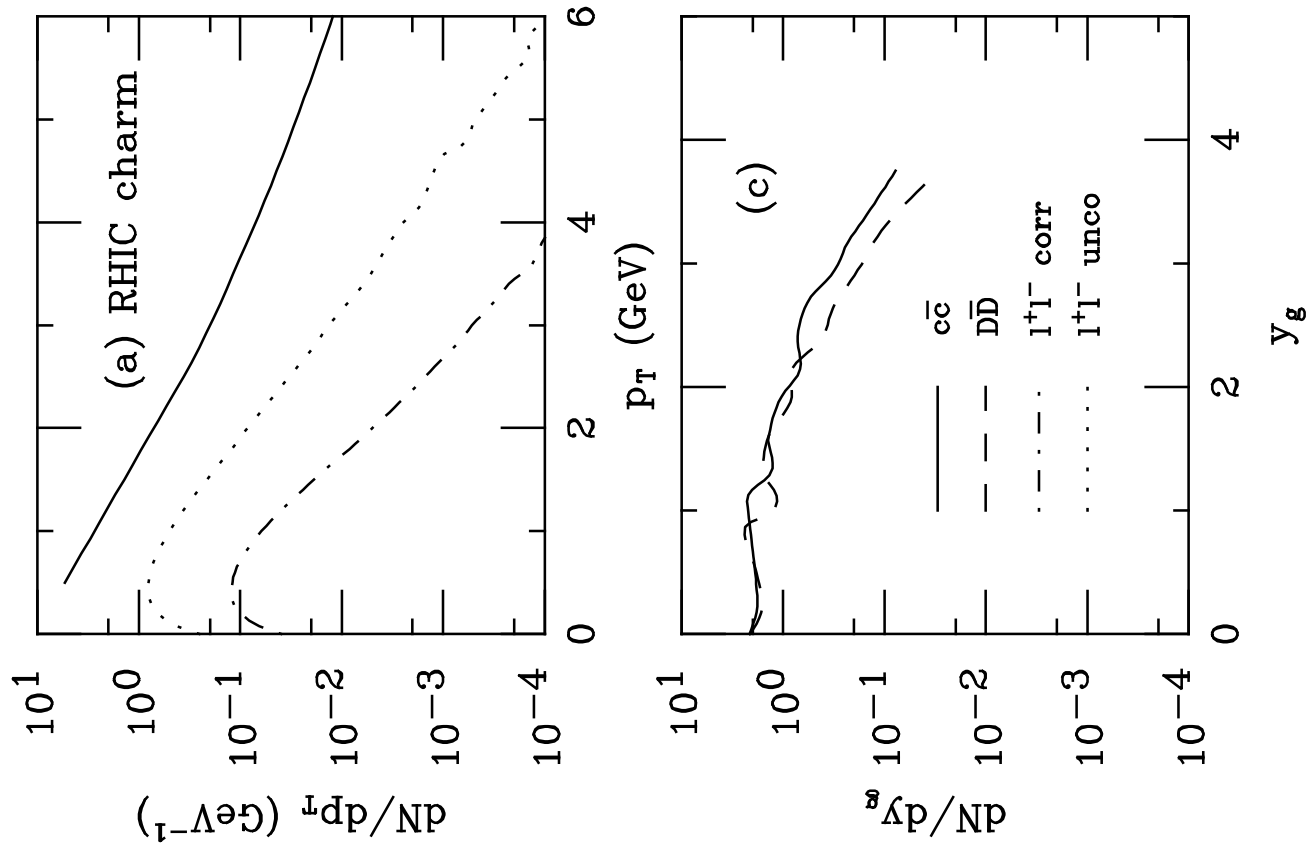


Figure 5

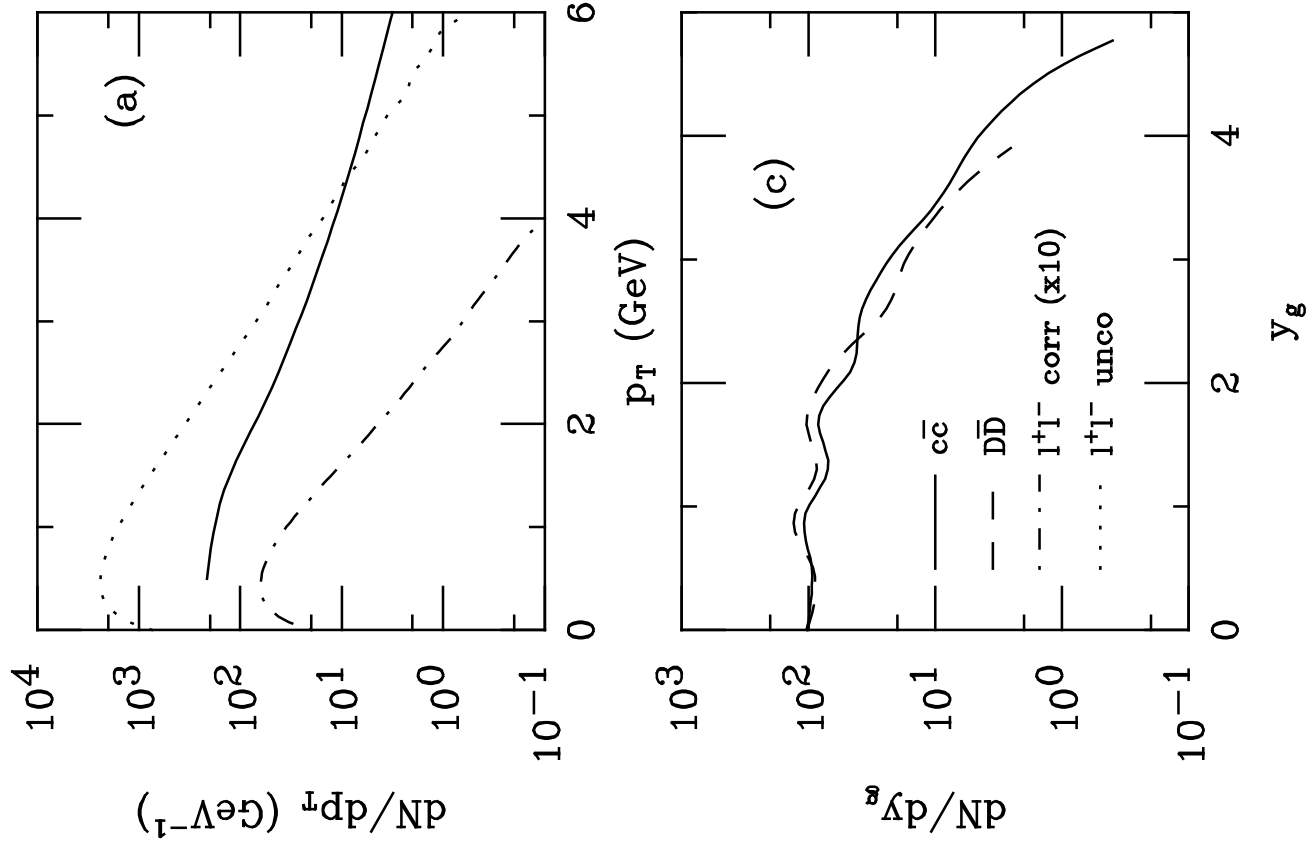


Figure 6

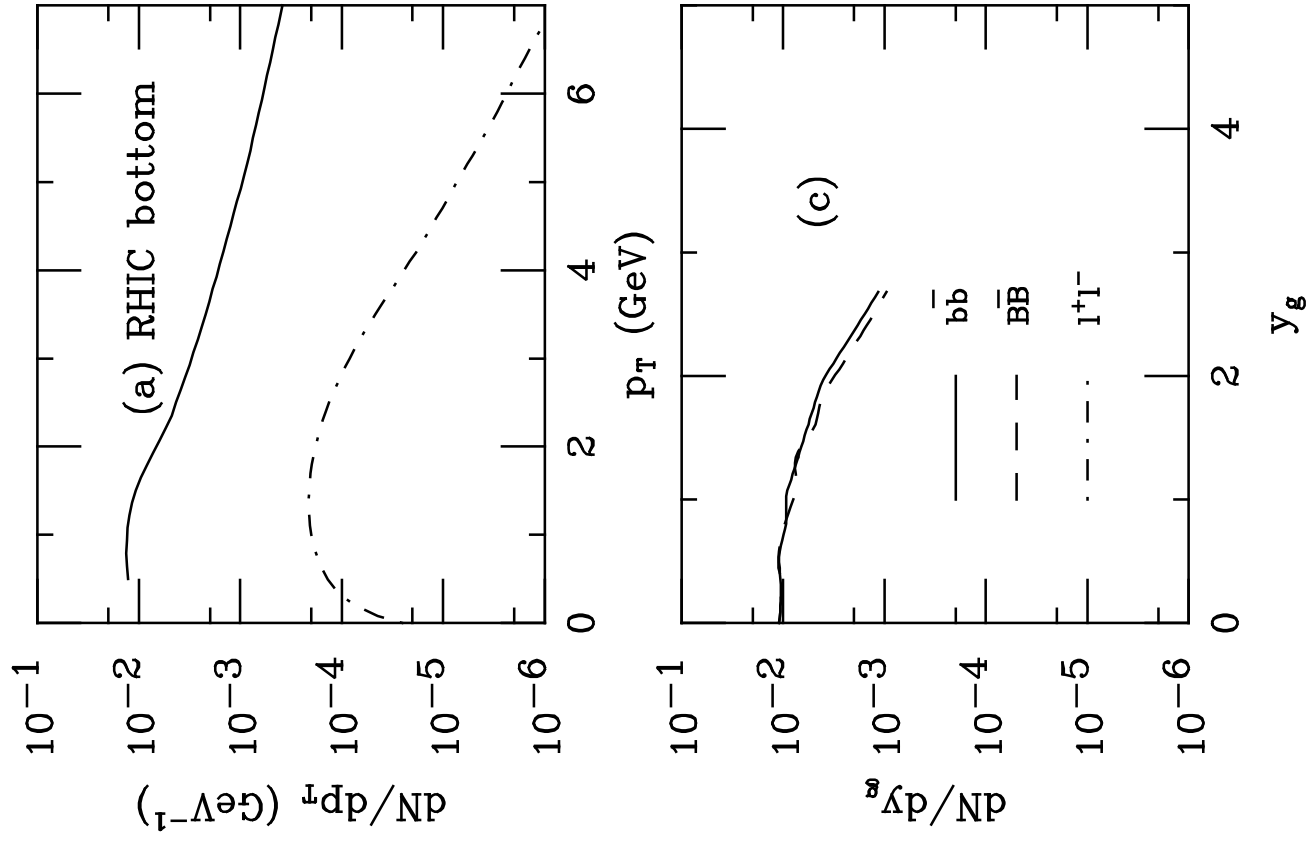


Figure 7

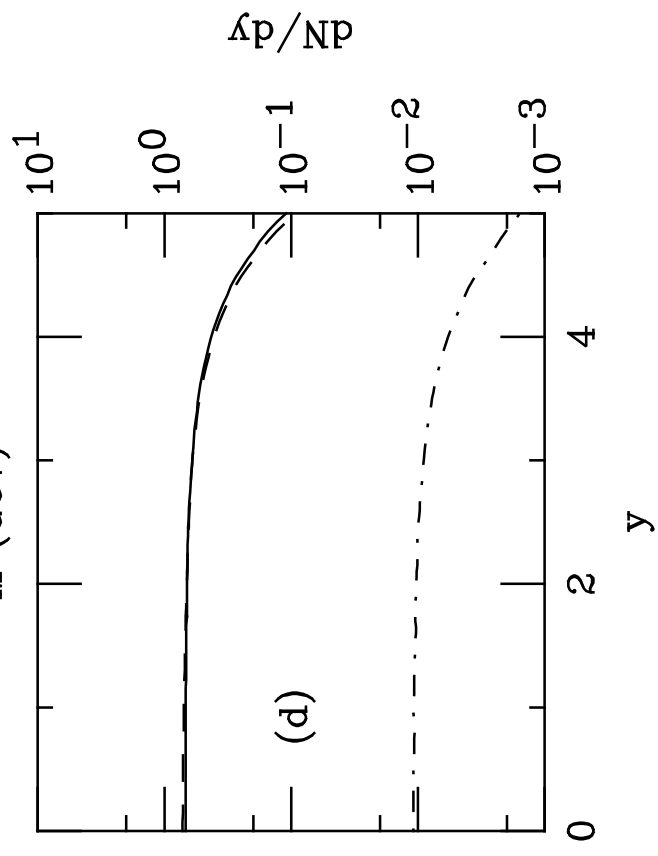
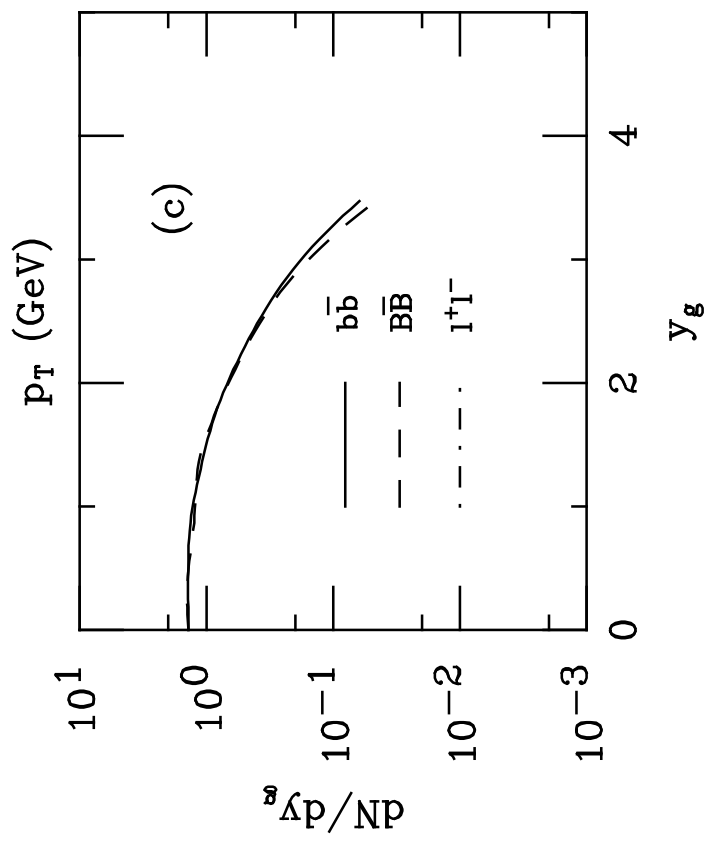
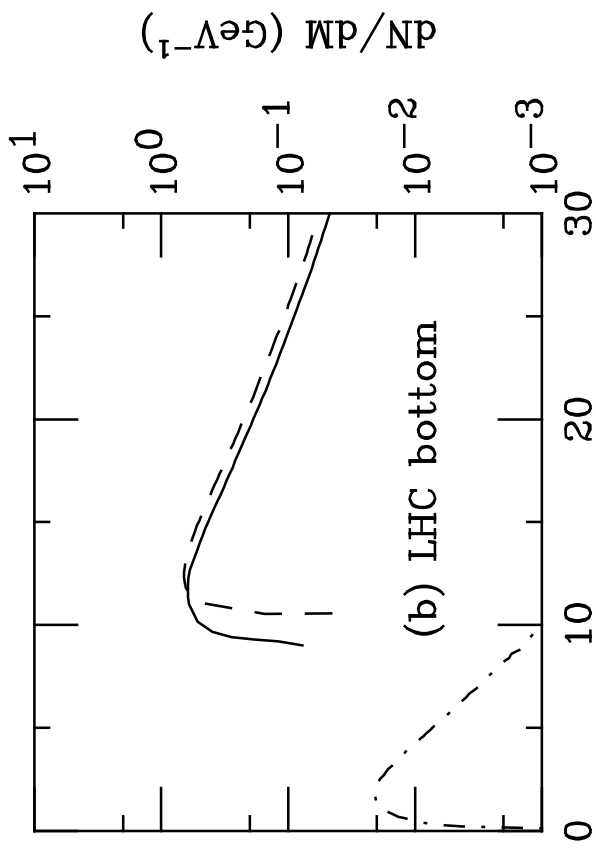
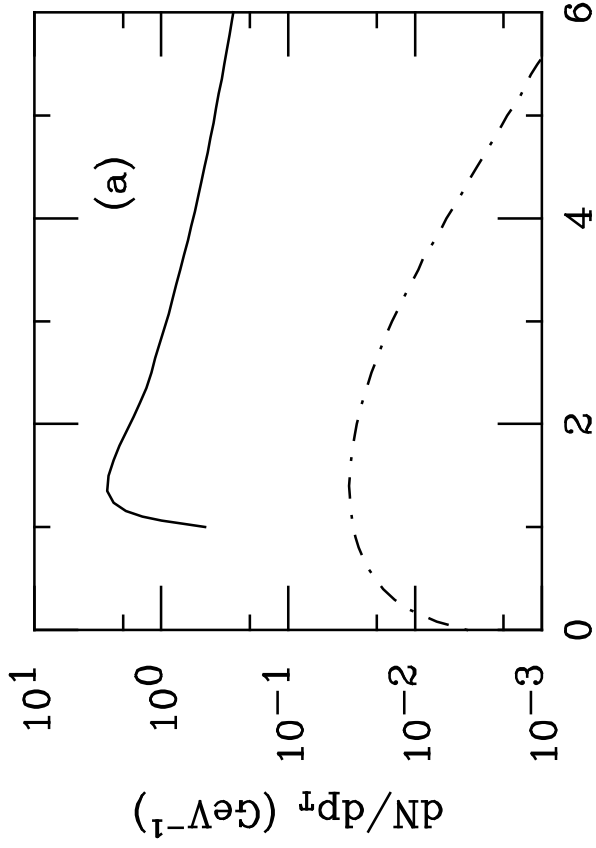


Figure 8

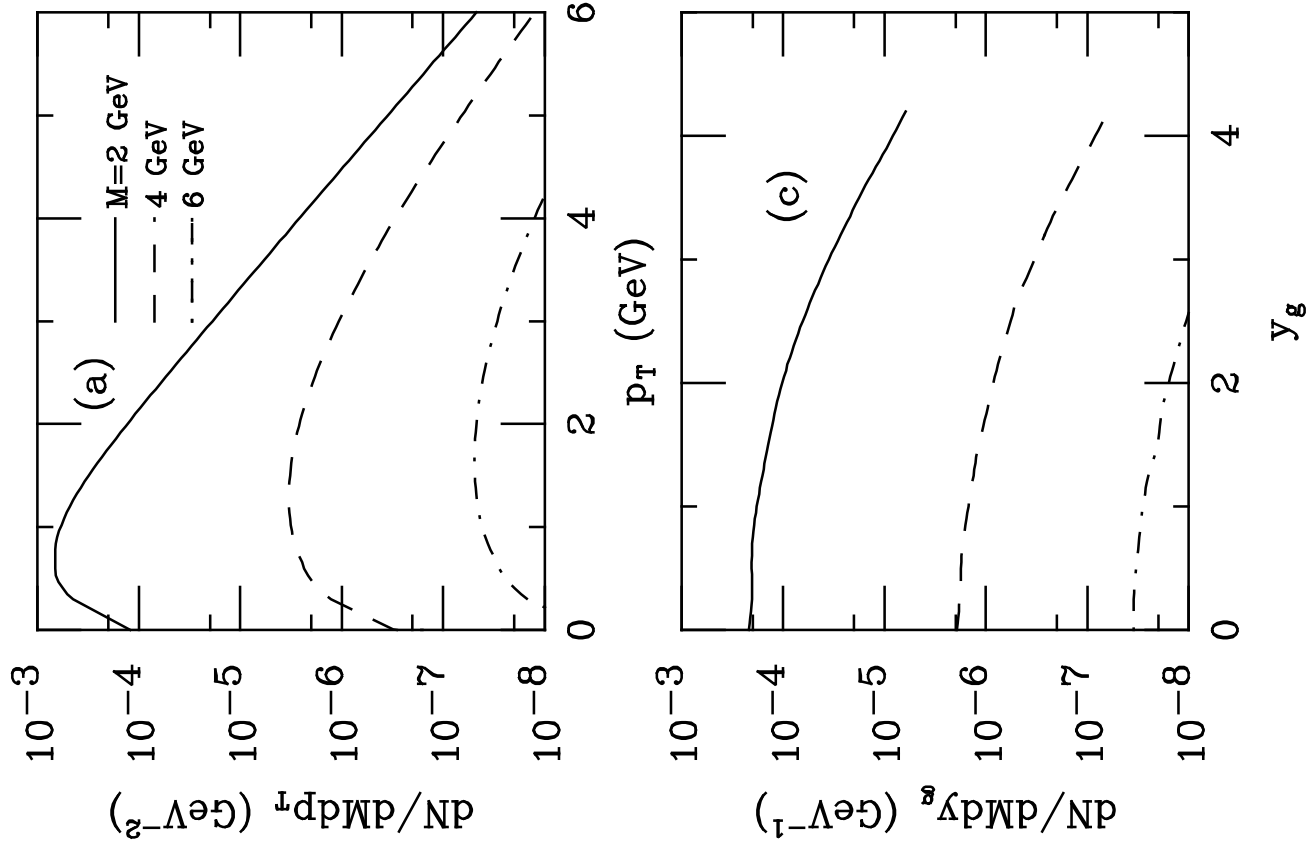


Figure 9

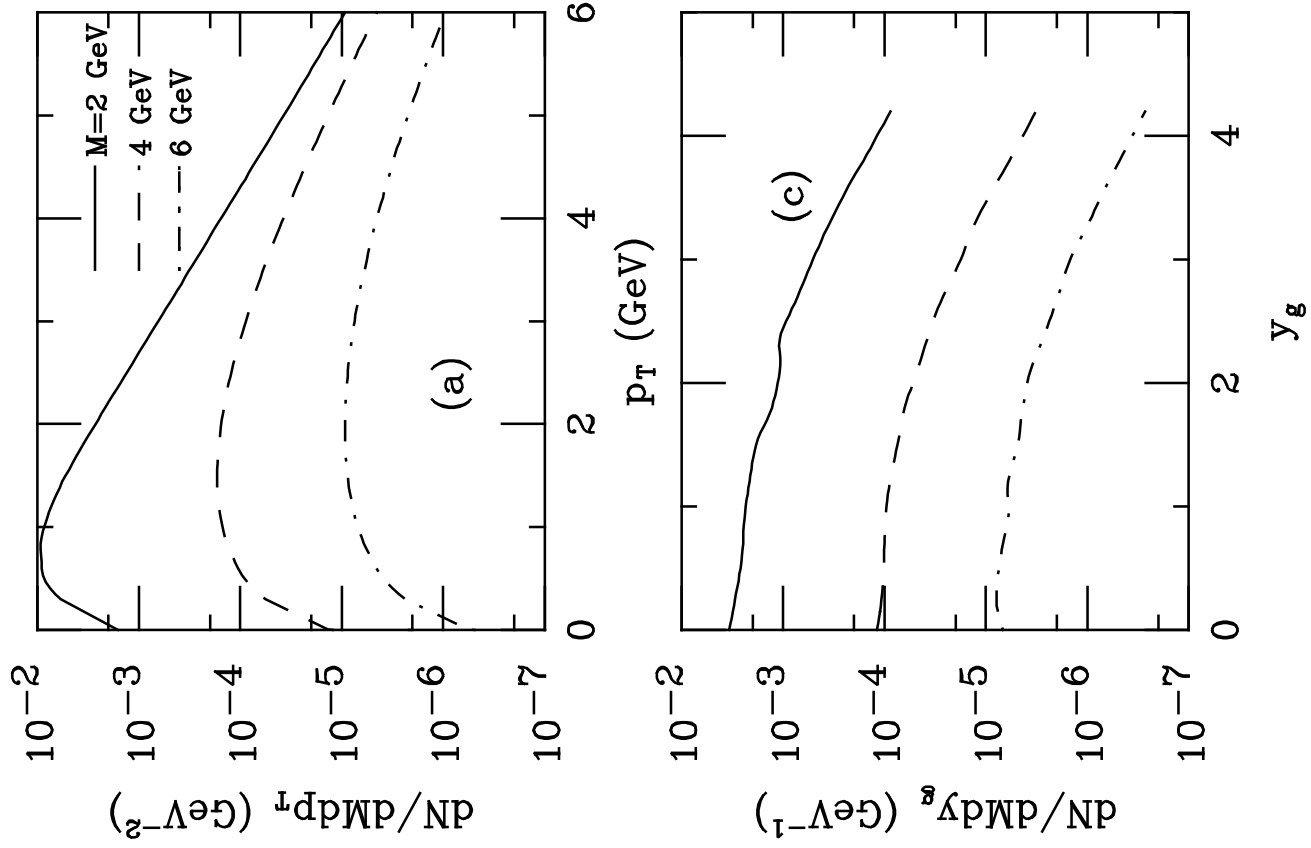


Figure 10

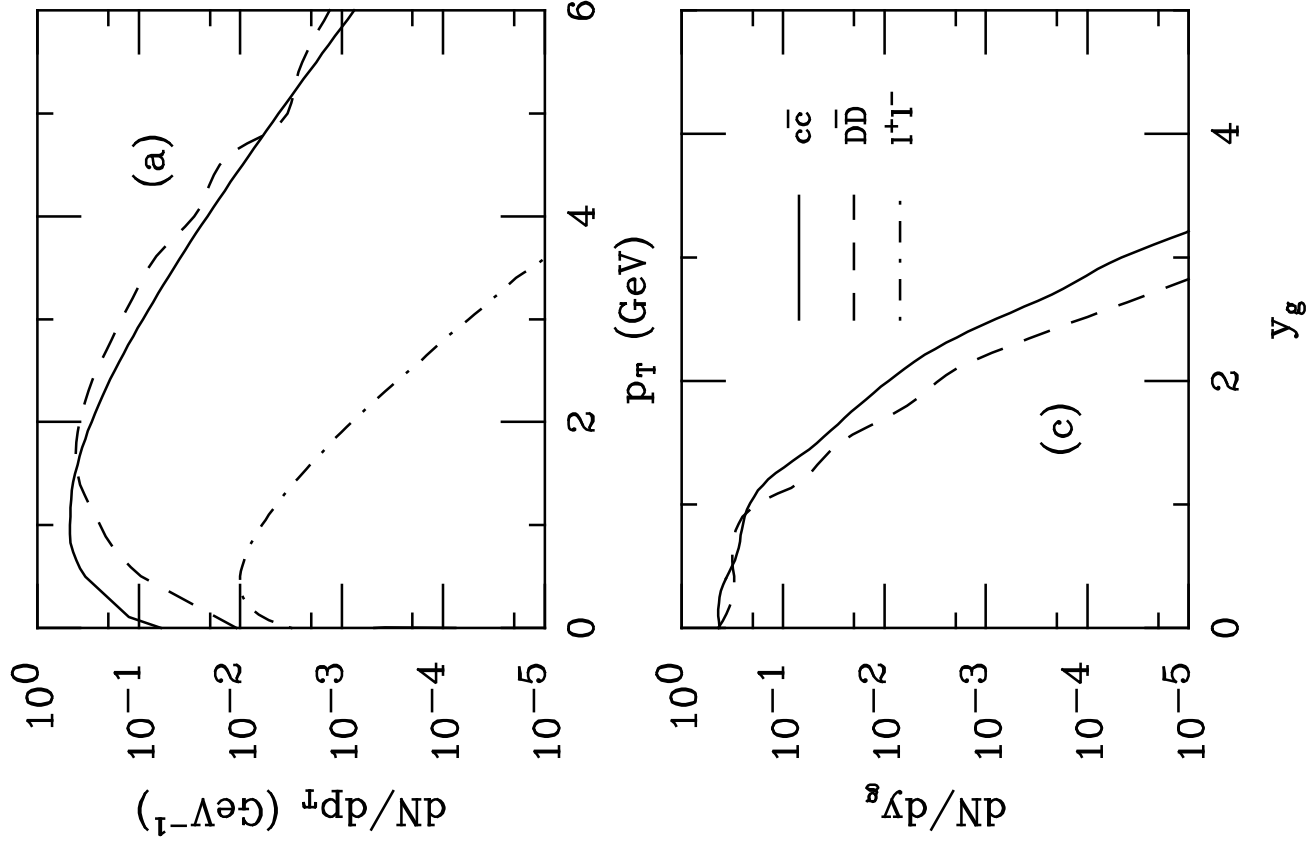


Figure 11

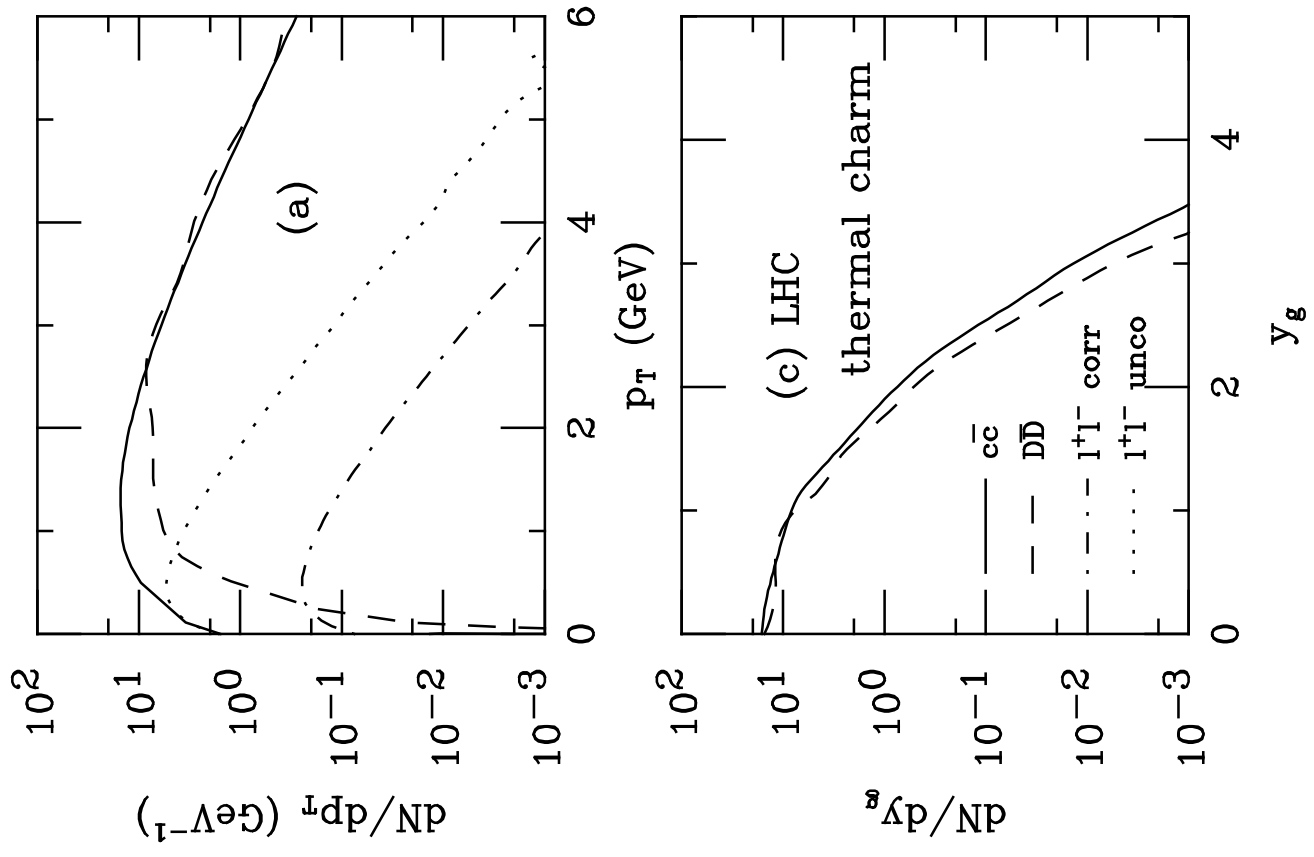


Figure 12

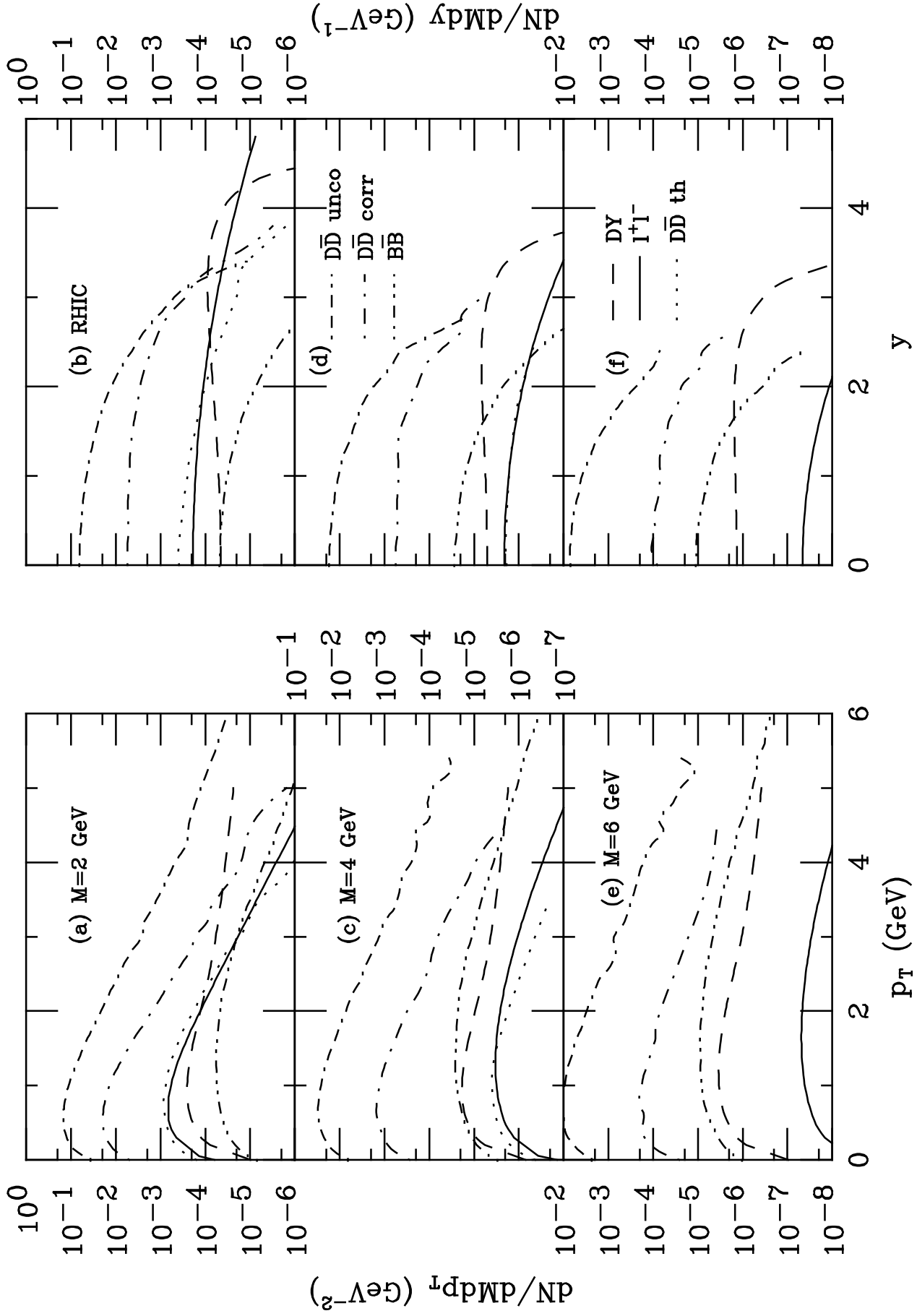


Figure 13

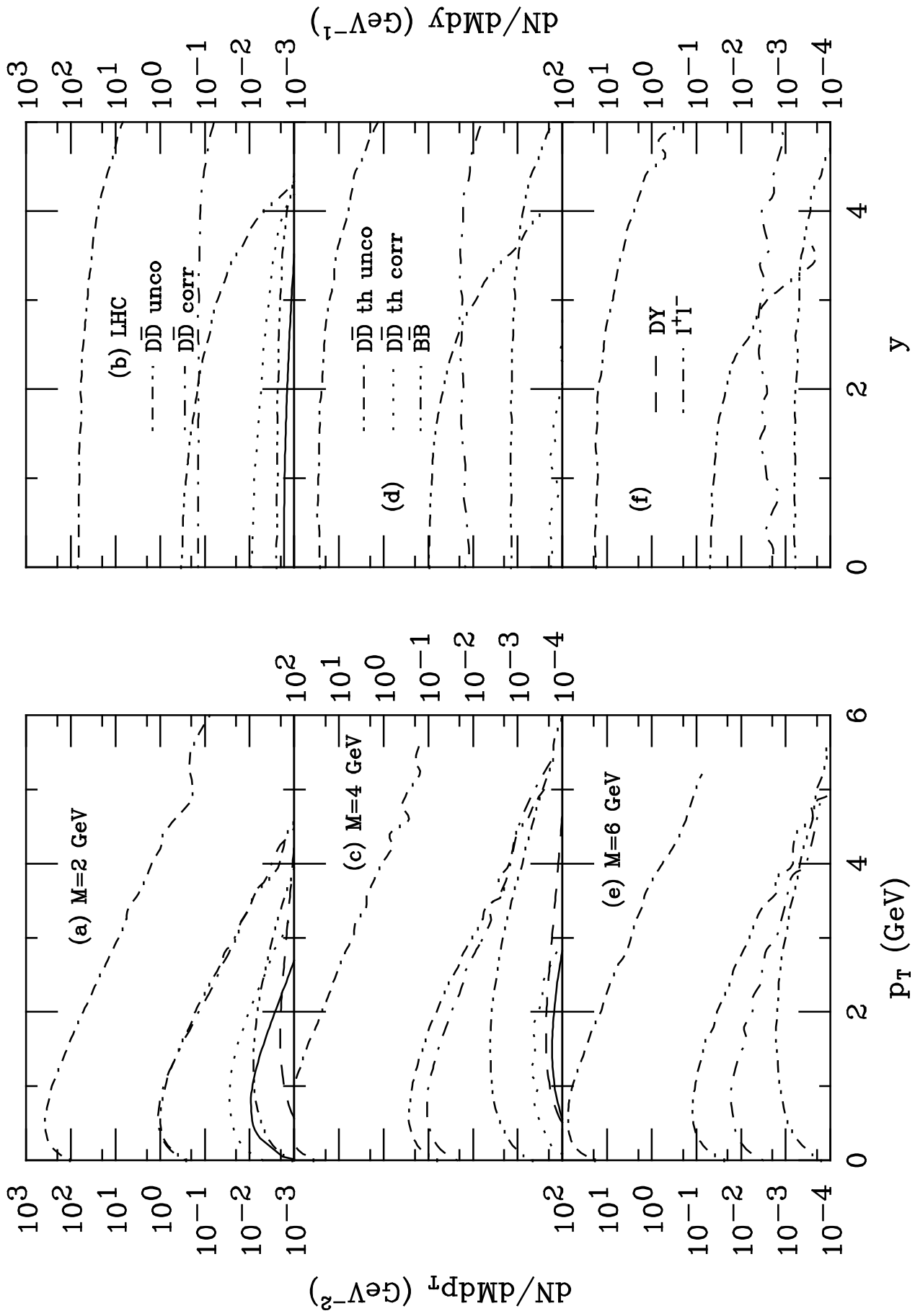


Figure 14

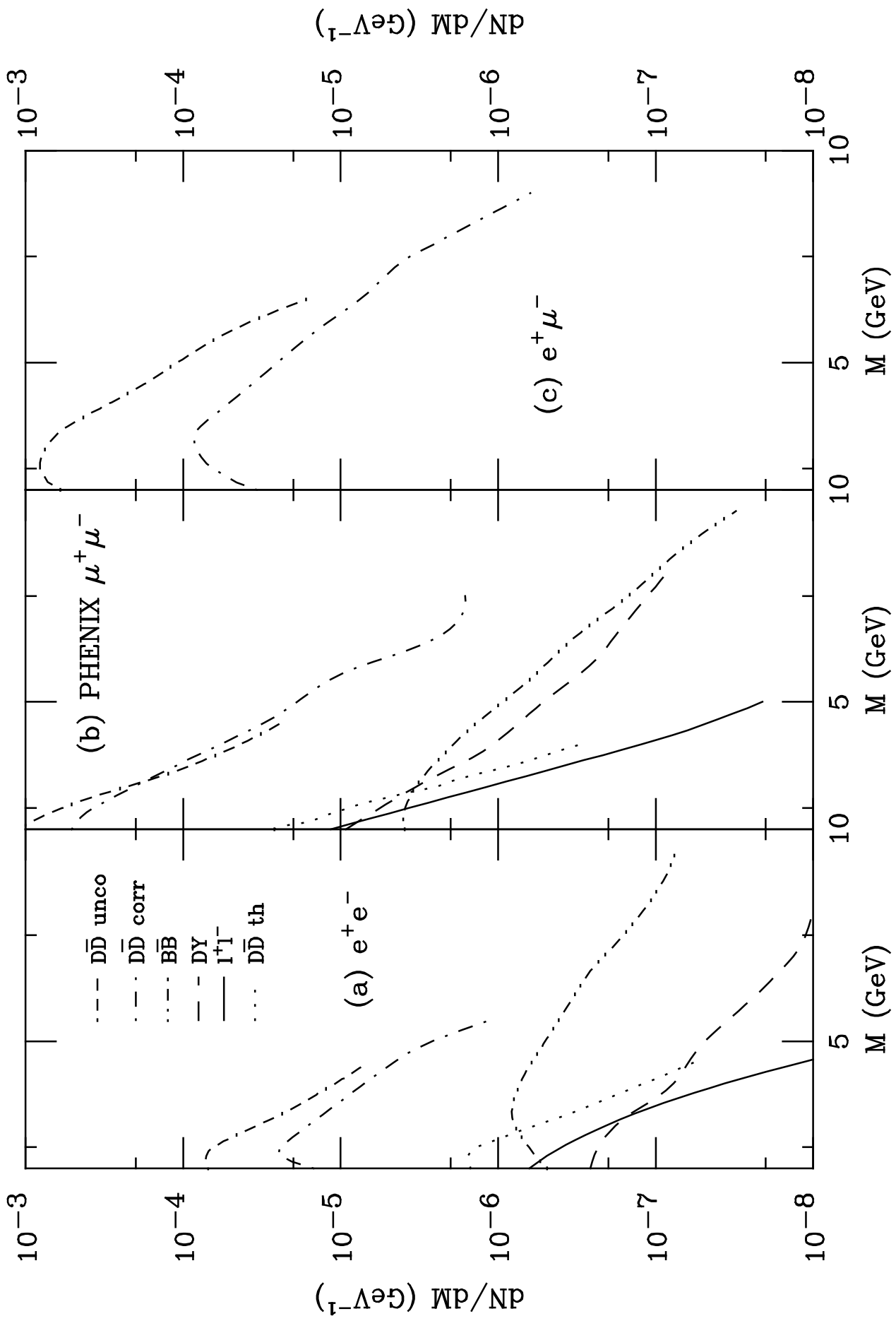


Figure 15

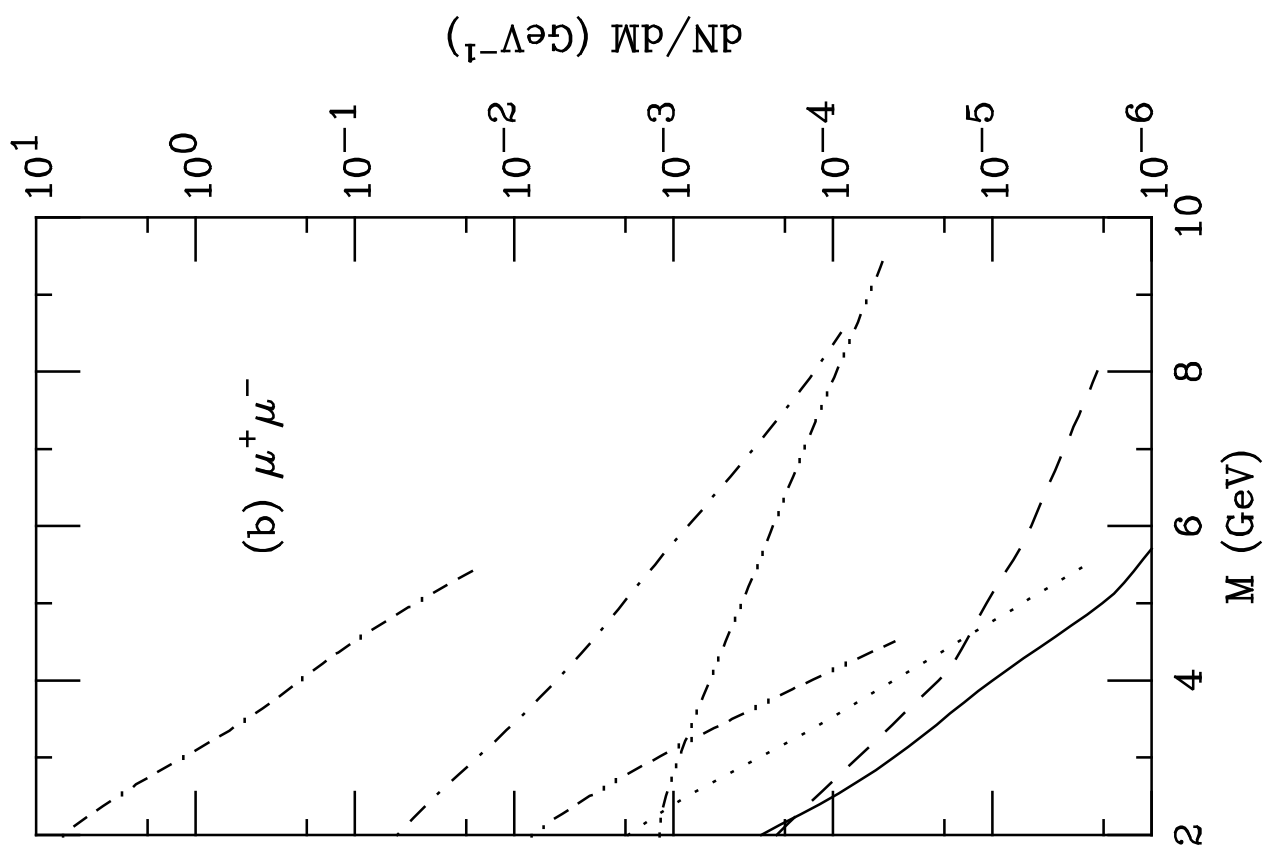
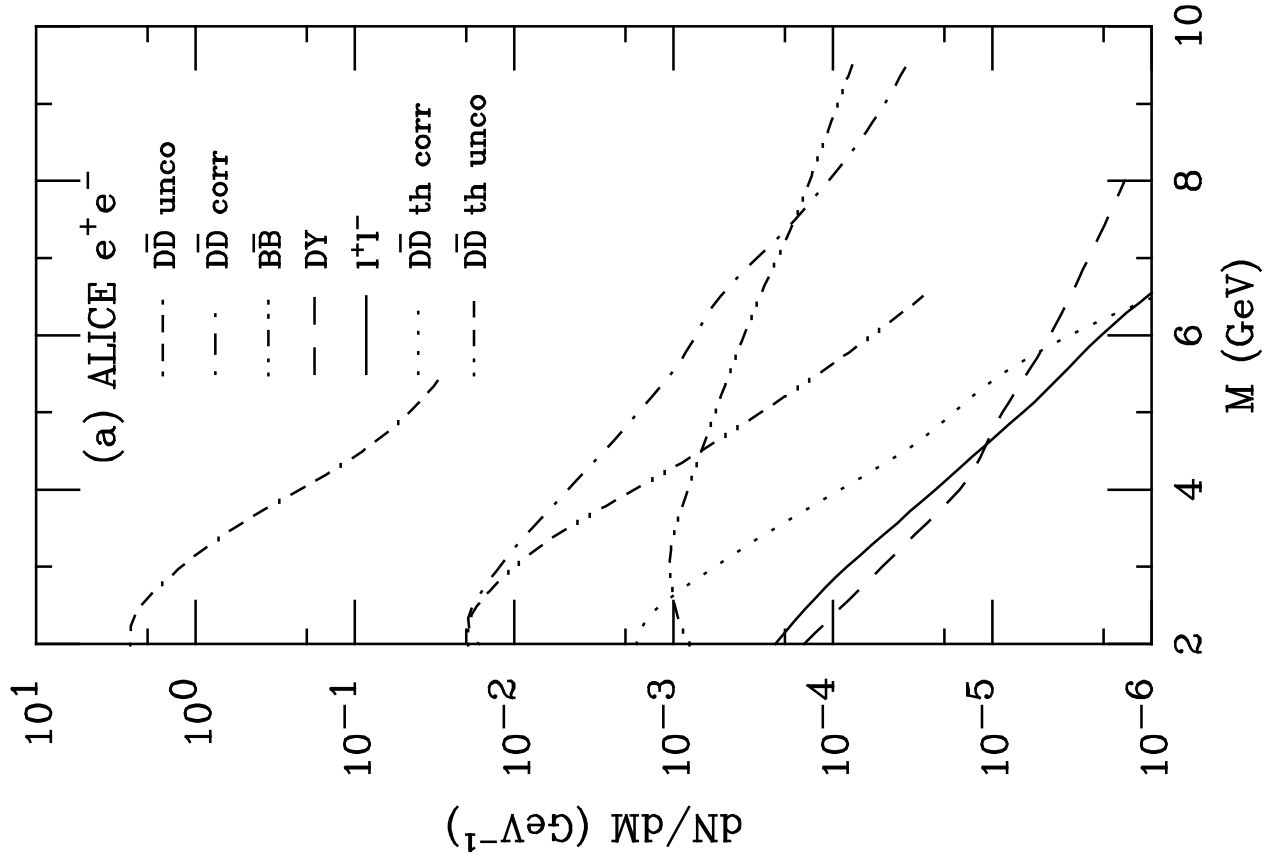


Figure 16

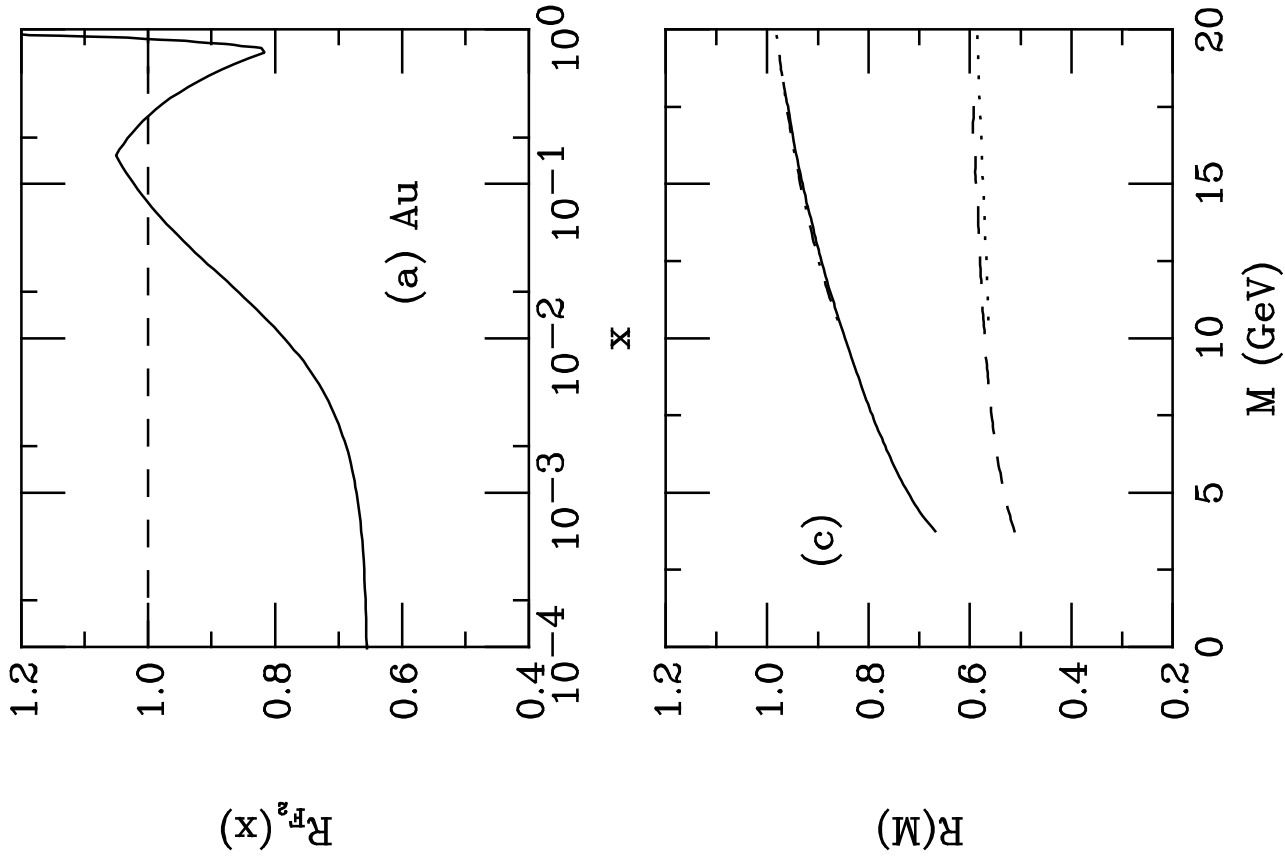


Figure 17

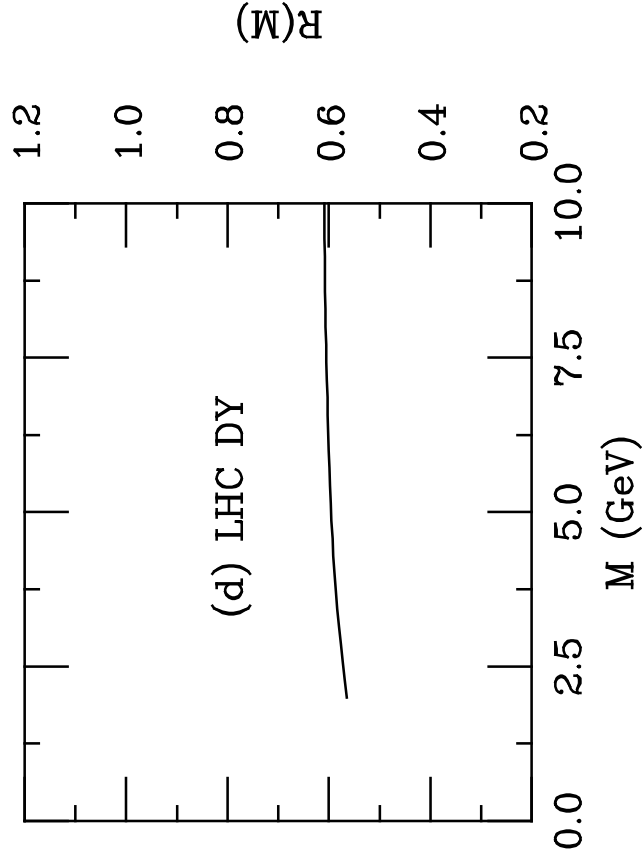
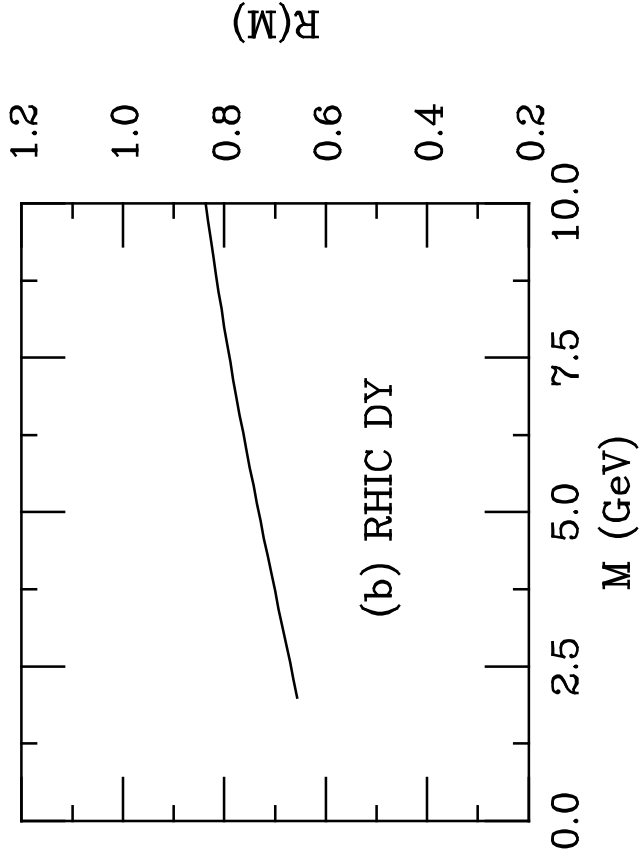
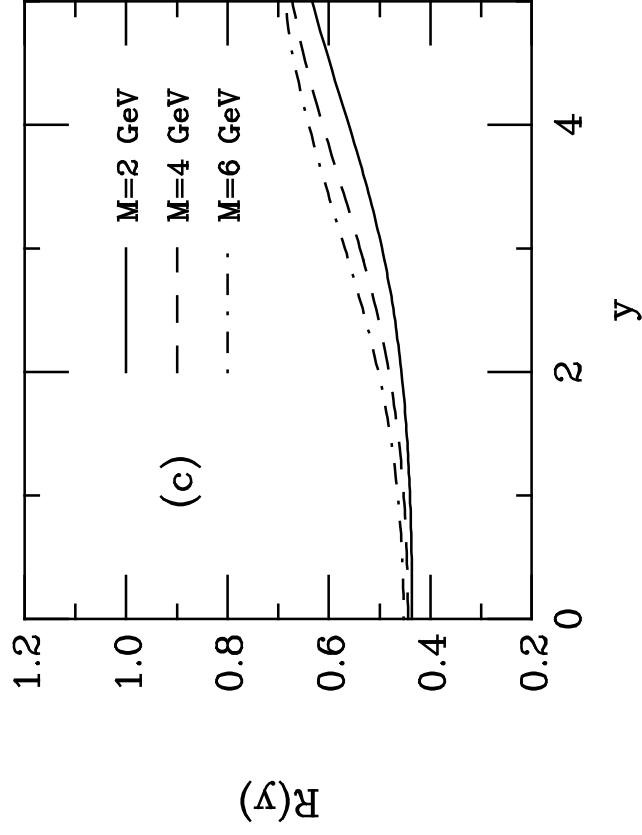
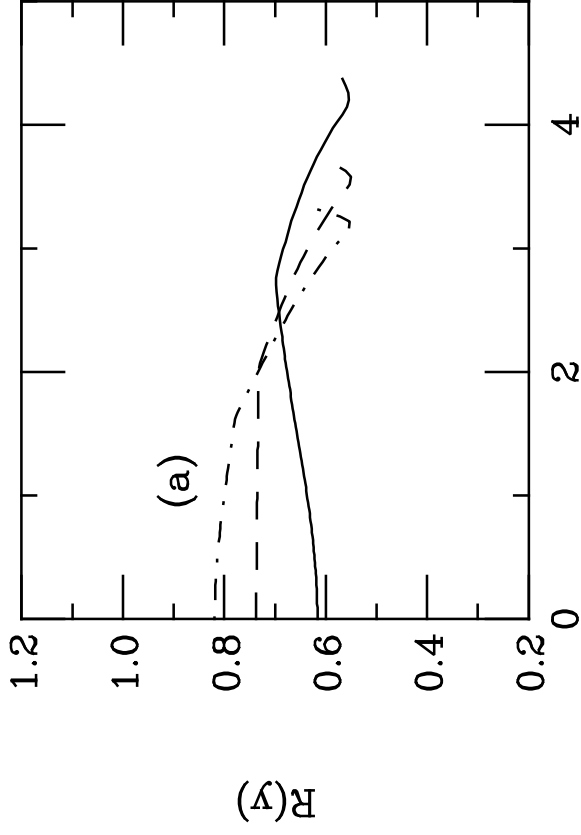


Figure 18

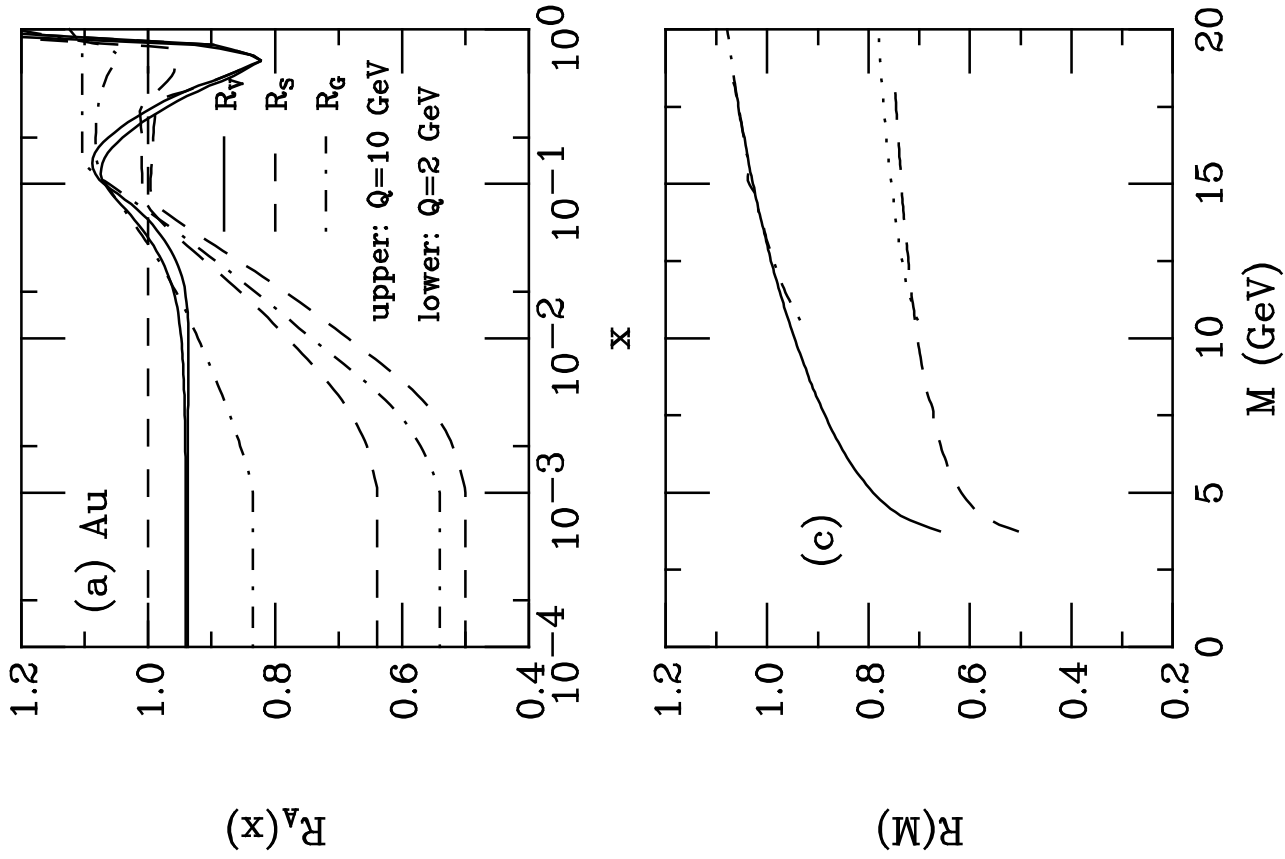


Figure 19

